

The 2dF Galaxy Redshift Survey: spherical harmonics analysis of fluctuations in the final catalogue

Will J. Percival,^{1*} Daniel Burkey,¹ Alan Heavens,¹ Andy Taylor,¹ Shaun Cole,² John A. Peacock,¹ Carlton M. Baugh,² Joss Bland-Hawthorn,³ Terry Bridges,^{3,4} Russell Cannon,³ Matthew Colless,³ Chris Collins,⁵ Warrick Couch,⁶ Gavin Dalton,^{7,8} Roberto De Propris,⁹ Simon P. Driver,⁹ George Efstathiou,¹⁰ Richard S. Ellis,¹¹ Carlos S. Frenk,² Karl Glazebrook,¹² Carole Jackson,¹³ Ofer Lahav,^{10,14} Ian Lewis,⁷ Stuart Lumsden,¹⁵ Steve Maddox,¹⁶ Peder Norberg,¹⁷ Bruce A. Peterson,⁹ Will Sutherland¹⁰ and Keith Taylor¹¹ (The 2dFGRS Team)

¹*Institute for Astronomy, University of Edinburgh, Royal Observatory, Blackford Hill, Edinburgh EH9 3HJ*

²*Department of Physics, University of Durham, South Road, Durham DH1 3LE*

³*Anglo-Australian Observatory, PO Box 296, Epping, NSW 2121, Australia*

⁴*Physics Department, Queen's University, Kingston, ON, K7L 3N6, Canada*

⁵*Astrophysics Research Institute, Liverpool John Moores University, Twelve Quays House, Birkenhead L14 1LD*

⁶*Department of Astrophysics, University of New South Wales, Sydney, NSW 2052, Australia*

⁷*Department of Physics, University of Oxford, Keble Road, Oxford OX1 3RH*

⁸*Space Science and Technology Division, Rutherford Appleton Laboratory, Chilton, Didcot OX11 0QX*

⁹*Research School of Astronomy & Astrophysics, The Australian National University, Weston Creek, ACT 2611, Australia*

¹⁰*Institute of Astronomy, University of Cambridge, Madingley Road, Cambridge CB3 0HA*

¹¹*Department of Astronomy, Caltech, Pasadena, CA 91125, USA*

¹²*Department of Physics & Astronomy, Johns Hopkins University, Baltimore, MD 21218-2686, USA*

¹³*CSIRO Australia Telescope National Facility, PO Box 76, Epping, NSW 1710, Australia*

¹⁴*Department of Physics and Astronomy, University College London, Gower Street, London WC1E 6BT*

¹⁵*Department of Physics, University of Leeds, Woodhouse Lane, Leeds LS2 9JT*

¹⁶*School of Physics & Astronomy, University of Nottingham, Nottingham NG7 2RD*

¹⁷*ETHZ Institut für Astronomie, HPF G3.1, ETH Hönggerberg, CH-8093 Zürich, Switzerland*

Accepted 2004 June 22. Received 2004 June 9; in original form 2004 April 20

ABSTRACT

We present the result of a decomposition of the 2dF Galaxy Redshift Survey (2dFGRS) galaxy overdensity field into an orthonormal basis of spherical harmonics and spherical Bessel functions. Galaxies are expected to directly follow the bulk motion of the density field on large scales, so the absolute amplitude of the observed large-scale redshift-space distortions caused by this motion is expected to be independent of galaxy properties. By splitting the overdensity field into radial and angular components, we linearly model the observed distortion and obtain the cosmological constraint $\Omega_m^{0.6}\sigma_8 = 0.46 \pm 0.06$. The amplitude of the linear redshift-space distortions relative to the galaxy overdensity field is dependent on galaxy properties and, for L_* galaxies at redshift $z = 0$, we measure $\beta(L_*, 0) = 0.58 \pm 0.08$, and the amplitude of the overdensity fluctuations $b(L_*, 0)\sigma_8 = 0.79 \pm 0.03$, marginalizing over the power spectrum shape parameters. Assuming a fixed power spectrum shape consistent with the full Fourier analysis produces very similar parameter constraints.

Key words: cosmological parameters – large-scale structure of Universe.

1 INTRODUCTION

Analysis of galaxy redshift surveys provides a statistical measure of the surviving primordial density perturbations. These fluctuations have a well-known dependency on cosmological parameters

*E-mail: wjp@roe.ac.uk

(e.g. Eisenstein & Hu 1998), and can therefore be used to constrain cosmological models. The use of large-scale structures as cosmological probes has acquired an increased importance in the new era of high-precision cosmology, which follows high-quality measurements of the cosmic microwave background (CMB) power spectrum (Bennett et al. 2003; Hinshaw et al. 2003). The extra information from galaxy surveys helps to lift many of the degeneracies intrinsic to the CMB data and enhances the scientific potential of both data sets (e.g. Efstathiou et al. 2002; Percival et al. 2002; Spergel et al. 2003; Verde et al. 2003).

In this paper we decompose the large-scale structure density fluctuations observed in the 2dF Galaxy Redshift Survey (2dFGRS; Colless et al. 2001, 2003) into an orthonormal basis of spherical harmonics and spherical Bessel functions. In Percival et al. (2001, hereafter P01) we decomposed the partially complete 2dFGRS into Fourier modes using the method outlined by Feldman, Kaiser & Peacock (1994). In a companion paper (Cole et al., in preparation; hereafter C04) we analyse the final catalogue using Fourier modes. In P01 and C04, the Fourier modes were spherically averaged and fitted with model power spectra convolved with the spherically averaged survey window function. Redshift-space distortions destroy the spherical symmetry of the convolved power and potentially distort the recovered power from that expected with a simple spherical convolution. Analysis of mock catalogues presented in P01 and a detailed study presented in C04 showed that, in spite of these complications, cosmological parameter constraints can still be recovered from a basic Fourier analysis.

However, a decomposition into spherical harmonics and spherical Bessel functions rather than Fourier modes distinguishes radial and angular modes, and enables redshift-space distortions to be easily introduced into the analysis method (without the far-field approximation, Kaiser 1987), as well as allowing for the effects of the radial selection function and angular sky coverage (Heavens & Taylor 1995; hereafter HT). The downside is that spherical harmonic methods are, in general, more complex than Fourier techniques and are computationally more expensive. This is particularly apparent when only a relatively small fraction of the sky is to be modelled, as the observed modes are then the result of a convolution of the true modes with a wide window function. For nearly all sky surveys (e.g. *IRAS* surveys), correlations between modes are reduced, and the window is narrower leading to a reduced computational budget.

Consequently, a number of spherical harmonics decompositions have been previously performed for the *IRAS* surveys. The primary focus of much of the earlier work was the measurement of $\beta(L, z) \equiv \Omega_m(z)^{0.6}/b(L, z)$, a measure of the increased fluctuation amplitude caused by the linear movement of matter on to density peaks and out from voids (Kaiser 1987). Here $\Omega_m(z)$ is the matter density and $b(L, z)$ is a simplified measure of the relevant galaxy bias. See Berlind, Narayanan & Weinberg (2001) for a detailed study of $\beta(L, z)$ measurements assuming more realistic galaxy bias models.

For the *IRAS* 1.2-Jy survey, HT and Ballinger, Heavens & Taylor (1995) found $\beta \sim 1 \pm 0.5$ for fixed and varying power spectrum shapes, respectively, and similar constraints were also found by Fisher, Scharf & Lahav (1994) and Fisher et al. (1995). However, Cole, Fisher & Weinberg (1995) found $\beta = 0.52 \pm 0.13$ and Fisher & Nusser (1996) found $\beta = 0.6 \pm 0.2$ for the 1.2-Jy survey using the quadrupole-to-monopole ratio for the decomposition of the power spectrum into Legendre polynomials. No explanation for the apparent discrepancy between these results has yet been found, although we note that the results are consistent at approximately the 1- σ level if the large errors are taken into account for the spherical harmonics decompositions.

The *IRAS* Point Source Catalogue Redshift Survey (PSCz; Saunders et al. 2000) has also been analysed using a Spherical Harmonics decomposition by a number of authors (Tadros et al. 1999; Hamilton, Tegmark & Padmanabhan 2000; Taylor et al. 2001) who found $\beta \sim 0.4$. More recently, Tegmark, Hamilton & Xu (2002) presented an analysis using spherical harmonics to decompose the first 100-k redshifts released from the 2dFGRS and found $\beta = 0.49 \pm 0.16$ for the b_J selected galaxies in this survey, consistent with the $\xi(\sigma, \pi)$ analyses of Peacock et al. (2001) and Hawkins et al. (2003). The measured β constraints are expected to vary among samples through the dependence on the varying galaxy bias. For example, by analysing the bispectrum of the PSCz survey Feldman et al. (2001) found a smaller large-scale bias than a similar analysis of the 2dFGRS by Verde et al. (2002).

In addition to the linear distortions, random galaxy motions within galaxy groups produce the well-known Fingers of God effect where structures are elongated along the line of sight. These random motions mean that the observed power is a convolution of the underlying power with a narrow window. The observed power therefore depends on the form of this window and the amplitude of the velocity dispersion as a function of scale.

The 2dFGRS and Sloan Digital Sky Survey (SDSS; Abazajian et al. 2004) cover sufficient volume so that it is now possible to recover information about the shape of the power spectrum in addition to the redshift-space distortions (P01, Tegmark et al. 2002, 2003a, C04). However, the decreased random errors (cosmic variance) of these new measurements means that systematic uncertainties have become increasingly important. In particular, galaxies are biased tracers of the matter distribution: the relation between the galaxy and mass density fields is probably both non-linear and stochastic to some extent (e.g. Dekel & Lahav 1999), so that the power spectra of galaxies and mass differ in general. Assuming that the bias tends towards a constant on large scales, then we can write $P_g(k) = b^2 P_m(k)$, where the subscripts m and g denote matter and galaxies, respectively. For the 2dFGRS galaxies, although the average bias is close to unity (Lahav et al. 2002; Verde et al. 2002), the bias is dependent on galaxy luminosity (Norberg et al. 2001, 2002a; Zehavi et al. 2002 find a very similar dependence for SDSS galaxies), with $\langle b(L, z)/b(L_*, z) \rangle = 0.85 + 0.15L/L_*$ where the bias $b(L, z)$ is assumed to be a simple function of galaxy luminosity and L_* is defined such that $M_{b_J} - 5 \log_{10} h = -19.7$ (Norberg et al. 2002b). As average galaxy luminosity is a function of distance, this bias can distort the shape of the recovered power spectrum (Tegmark et al. 2003a; Percival, Verde & Peacock 2004).

In this paper we decompose the final 2dFGRS catalogue into an orthonormal basis of spherical harmonics and spherical Bessel functions and fit cosmological models to the resulting mode amplitudes. To compress the modes we adopt a modified Karhunen–Loève (KL) data-compression method that separates angular and radial modes (Vogeley & Szalay 1996; Tegmark, Taylor & Heavens 1997; Hamilton et al. 2000; Tegmark et al. 2002). We also include a consistent correction for luminosity-dependent bias that includes the effect of this bias on both the measured power and the fitted models. We have performed two fits to the recovered modes. First we measured the galaxy power spectrum amplitude, $b(L_*, 0)\sigma_8$ and the linear infall amplitude, $\beta(L_*, 0)$ for a fixed power spectrum shape. We then considered fitting a more general selection of cosmological models to these data.

A detailed analysis of the internal consistency of the 2dFGRS catalogue with respect to measuring $P(k)$ was performed using a Fourier decomposition of the galaxy density field and is presented in C04. This analysis included looking at the effect of changing the

calibration, maximum redshift, weighting, region and galaxy colour range considered. This work is not duplicated using our decomposition technique, and we instead refer the interested reader to that paper. Tests presented in this paper are primarily focused on the analysis method, although we consider the effect of the catalogue calibration in Section 6.

The layout of this paper is as follows. In Section 2 we describe the 2dFGRS catalogue analysed, and in Section 3 we consider mock catalogues used to test our analysis method. A brief overview of the methodology is presented in Section 4. A full description of the spherical harmonics method used is provided in Appendix A. The results are presented for both the 2dFGRS and the mock catalogues in Sections 5.2 and 5.3. A discussion of various tests performed is given in Section 6. We conclude in Section 7.

2 THE 2DFGRS CATALOGUE

In this work, we consider the final 2dFGRS release catalogue. However, the formalism adopted is simplified if we consider a catalogue with a selection function that is separable in the radial and angular directions (see Appendix A for details of the formalism). There are two complications in the 2dFGRS catalogue that cause departures from such behaviour (as discussed in Colless et al. 2001, 2003) as follows.

(i) The photometric calibration of the UK Schmidt Telescope plates from which the 2dFGRS sample was drawn and the extinction correction have been revised after the initial sample selection. As revision of the galaxy magnitudes and the angular magnitude limit are required, this means that the survey depth varies across the sky.

(ii) Due to seeing variations between observations, the overall completeness varies with apparent magnitude with a form that depends on the field redshift completeness. This is characterized by a parameter μ , with the varying completeness given by $c_z(m, \mu) = 0.99[1 - \exp(m - \mu)]$ (Colless et al. 2001).

Rather than adapt the formalism, we have chosen to use a reduced version of the 2dFGRS release catalogue with a window function that is separable in the radial and angular directions. These issues were also discussed with reference to the 100-k release catalogue by Tegmark et al. (2002) whose method also required a sample with window function and weights separable in the radial and angular directions. Correcting for these effects is relatively straightforward, if a little painful as we have to remove galaxies with valid redshifts from the analysis. First we need to select a uniform revised magnitude limit at which to cut the catalogue. Galaxies fainter than this limit are removed from the revised catalogue, as are galaxies that were selected using an actual magnitude limit that was brighter than the revised limit. Selecting the revised magnitude limit at which to cut the catalogue is a compromise between covering as large an angular region as possible (resulting in a narrow angular window function), covering as large a weighted volume as possible (reducing cosmic variance) or retaining as many galaxies as possible (reducing shot noise). However, we can model variations in the angular window function and, in Percival et al. (2001), we showed that the 2dFGRS sample is primarily cosmic variance limited. We therefore chose the magnitude limit to maximize the effective volume of the survey.

The random fields, a number of circular 2-deg fields randomly placed in the low-extinction regions of the southern automated plate measurement (APM) galaxy survey were excluded from our analysis, in order to focus on two contiguous regions with well-behaved selection functions. These two regions of the survey, one near the

Table 1. Limiting extinction-corrected magnitudes, numbers of galaxies, and assumed radial selection-function parameters for each of the two 2dFGRS regions modelled. The parameters controlling the radial distribution are defined by equation (1).

region	M_{lim}	N_{gal}	z_c	b	g
SGP	19.29	84824	0.130	2.21	1.34
NGP	19.17	57932	0.128	2.45	1.24

North Galactic Pole (NGP) and another near the South Galactic Pole (SGP) were analysed separately, and optimization of the magnitude limit was performed for each region independently. The resulting limits are given in Table 1. To correct for the magnitude-dependent completeness, we removed a randomly selected sample of the bright galaxies in order to provide uniform completeness as a function of magnitude.

The redshift distribution of each sample was matched using a function of the form

$$f(z) \propto z^g \exp \left[- \left(\frac{z}{z_c} \right)^b \right], \quad (1)$$

where the parameters z_c , b and g were calculated by fitting to the weighted (equation A5) redshift distribution, calculated in 40 bins equally spaced in z . These resulting parameter values are given in Table 1, and the redshift distributions are compared with the fits in Fig. 1. In addition to the radial and angular distributions of the sample, we also need to match the normalization of the catalogue to the expected distribution. We choose to normalize each catalogue by matching $\int d\mathbf{r} \bar{n}(\mathbf{r}) w(\mathbf{r})$, where $\bar{n}(\mathbf{r})$ is the expected galaxy distribution function and $w(\mathbf{r})$ is the weight applied to each galaxy (equation A5), for reasons described in Percival et al. (2004).

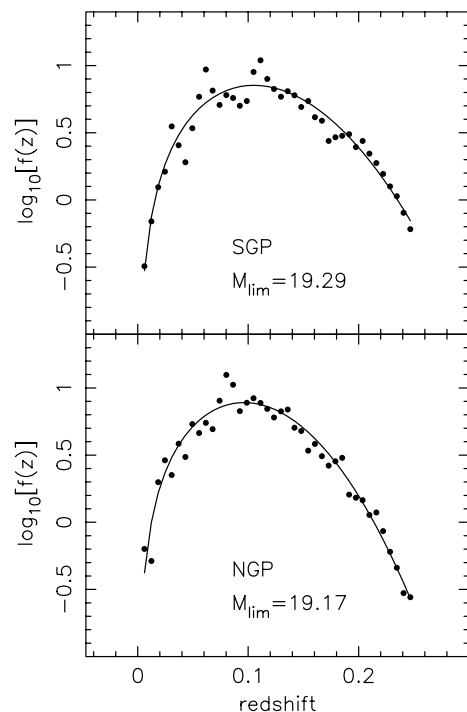


Figure 1. Redshift distribution of the reduced galaxy catalogues for the two regions considered (solid circles), compared with the best-fitting redshift distribution for each of the form given by equation (1). The magnitude limit adopted for each sample is given in each panel.

3 THE MOCK CATALOGUES

As a test of the spherical harmonics procedure adopted, we have applied our method to recover parameters from the 22 LCDM03 Hubble Volume mock catalogues available from <http://star-www.dur.ac.uk/~cole/mocks/main.html> (Cole et al. 1998). These catalogues were calculated using an empirically motivated biasing scheme to place galaxies within N -body simulations, and were designed to cover the 2dFGRS volume. We have applied the same magnitude and completeness cuts to these data, as applied to the 2dFGRS catalogue (Section 2). In order to allow for slight variations between the redshift distribution of the mocks and the 2dFGRS catalogue, we fit the redshift distribution of the mock catalogues independently from the 2dFGRS data. Because we adopt the magnitude limits used for the 2dFGRS data, the NGP and SGP regions in the mock catalogues have different redshift distributions and these are fitted separately. For simplicity, we assume a single expected redshift distribution for each region for all of the mocks, calculated by fitting to the redshift distribution a combination of all of the mocks. The number of galaxies in each catalogue is sufficient that the model of $f(z)$ only changes slightly when considering catalogues individually or the combination of all 22 catalogues. This change is sufficiently small so that it does not significantly alter either the recovered parameters from the mock catalogues or their distribution.

We use these mock catalogues in a number of ways. By comparing the average recovered parameters and known input parameters of the simulations, we test for systematic problems with the method. In fact, we did not analyse the 2dFGRS data until we had confirmed the validity of the method through application to these mock catalogues. We test our recovery of the linear redshift-space distortion parameter $\beta(L_*, z)$ by analysing mocks within the galaxy peculiar velocities that were altered (Section 6.7). Additionally, we use the distribution of recovered values to test the confidence intervals that we can place on recovered parameters (Section 5.4).

4 METHOD OVERVIEW

The use of spherical harmonics to decompose galaxy surveys dates back to Peebles (1973), and is a powerful technique for statistically analysing the distribution of galaxies. The formalism used in this paper is based in part on that developed by HT and described by Tadros et al. (1999). However, there are some key differences and extensions, which warrant the full description given in Appendix A. In this section we outline the procedure for a non-specialist reader.

The galaxy density field was decomposed into an orthonormal basis consisting of spherical Bessel functions and spherical harmonics. In general, we refer to this as a spherical harmonics decomposition. As in P01 and C04, we decomposed the density field in terms of proper distance and therefore needed to assign a radial distance to each galaxy. For this, we adopted a flat cosmology with $\Omega_m = 0.3$ and $\Omega_\Lambda = 0.7$. The dependence of the recovered power spectrum and $\beta(L_*, z)$ on this ‘prior’ is weak, and was explored in P01. We assume a constant galaxy clustering (CGC) model, where the amplitude of galaxy clustering is independent of redshift, although it is dependent on galaxy luminosity through the relation of Norberg et al. (2001) given in equation (A1). This relates the clustering amplitude of galaxies of luminosity L to that of L_* galaxies, and by weighting each galaxy by the reciprocal of this relation, we correct for any luminosity-dependent bias.

The spherical harmonics decomposition of the mean expected distribution of galaxies is then subtracted, calculated using a fit to

the radial distribution and an angular mask (this was modelled using a random catalogue in the Fourier analyses of P01 and C04). This converts from a decomposition of the density field to the overdensity field.

In the Fourier-based analyses of P01 and C04, we modelled the power spectrum observed. In the analysis presented in this paper we instead model the transformed overdensity field. The expected value of the transform of the overdensity field for any cosmological model is zero by definition. Consequently, apart from a weak dependence on a prior cosmological model hard-wired into the analysis method, the primary dependence on cosmological parameters is encapsulated in the covariance matrix used to determine the likelihood of each model.

The primary difficulty in calculating the covariance matrix for a given cosmological model is correctly accounting for the geometry of the 2dFGRS sample. This results in a significant convolution of the true power, and is performed as a discrete sum over spherical harmonic modes in a computationally intensive part of the adopted procedure. To first order, the large-scale redshift-space distortions are linearly dependent on the density field, and we can therefore split the covariance matrix into four components corresponding to the mass–mass, mass–velocity and velocity–velocity power spectra (cf. Tegmark et al. 2002, 2003a) and the shot noise. This is discussed after equation (A31) in Appendix A. The velocity component of the covariance matrix is dependent on the matter density field rather than the galaxy density field, and we include a correction for the linear evolution of this field. For this we assume that $\Omega_m = 0.3$ and $\Omega_\Lambda = 0.7$ although the resulting covariance matrix is only weakly dependent on this ‘prior’.

We include the contribution from the small-scale velocity dispersion of galaxies by undertaking an additional convolution of the radial component of these matrices. We choose to model scales where the small-scale velocity dispersion does not contribute significantly to the overdensity field, and demonstrate this weak dependence in Section 6.5.

The transformation between Fourier modes and spherical harmonics is unitary, so each spherical harmonic mode corresponds directly to a particular Fourier wavelength. Within our chosen decomposition of the density field, there are 86 667 spherical harmonic modes with $0.02 < k < 0.15 h \text{ Mpc}^{-1}$, and it is impractical to use all of these modes in a likelihood analysis as the inversion of an $86\,667 \times 86\,667$ matrix is slow and may be unstable for a problem such as this. The modes were therefore compressed, leaving 1223 and 1785 combinations of modes for the NGP and SGP, respectively. The data-compression procedure adopted was designed to remove nearly degenerate modes, which could cause numerical problems, and to optimally reduce the remaining data. The compressed data, and the corresponding covariance matrices are then combined to calculate the likelihood of a given model assuming Gaussian statistics.

Only ~ 5 per cent of the computer code used in the PSCz analysis of Tadros et al. (1999) was reused in the current work, as both revision of the method and a significant speeding up of the process were required to model the 2dFGRS. In particular, the geometry of the 2dFGRS sample means that the convolution to correct for the survey window function requires calculation for a larger number of modes than all-sky surveys such as the PSCz, and the method consequently takes longer to run. As a result of this revision, the method required thorough testing, by both analysing mock catalogues and considering the specific tests described in Section 6.

5 RESULTS

The results are presented for the 2dFGRS catalogue described in Section 2 and for the mock catalogues described in Section 3. The parameter constraints were derived by fitting to modes with $0.02 < k < 0.15 h \text{ Mpc}^{-1}$; the range considered in P01. As the spherical harmonics method includes the effects of the small-scale velocity dispersion and uses a non-linear power spectrum, we could, in principle, extend the fitted k range to smaller scales. However, our derivation of the covariance matrix is only based on cosmic variance and shot noise. No allowance is made for systematic offsets caused by our modelling of small-scale effects (velocity dispersion, non-linear power and a possible scale-dependent galaxy bias). Consequently, it is better to avoid regions in k space that are significantly affected by these complications, rather than assume that we can model these effects perfectly. Additionally, the number of modes that can be analysed is limited by computation time and the large-scale k -range selected includes most of the cosmological signal and follows Gaussian statistics.

The spherical harmonics method involves a convolution of the window and the model power over a large number of modes (equation A22). For a fixed power spectrum shape, the covariance matrix can be written as a linear sum of four components with different dependence on $b(L_*, 0)\sigma_8$ and $\beta(L_*, 0)$. It is straightforward to store these components and these parameters can be fitted without having to perform the convolution for each set of parameters. In Section 5.2 we consider a fixed power spectrum shape, and present results fitting $b(L_*, 0)\sigma_8$ and $\beta(L_*, 0)$ to the 2dFGRS and mock catalogue data.

In an analysis of the power spectrum shape, separate convolutions are required for each model $P(k)$. This would be computationally very expensive, but can be circumvented by discretizing the model $P(k)$ in k and performing a single convolution for each k component. In Section 5.3 we fit to the power spectrum shape, assuming a step-wise $P(k)$ in this way. First, we describe the set of models to be considered.

5.1 Cosmological parameters

A simple model is assumed for galaxy bias, with the galaxy overdensity field assumed to be a multiple (the bias $b[L, 0]$) of the present-day mass density field

$$\delta(L, \mathbf{r}) = b(L, 0)\delta(\text{mass}, \mathbf{r}), \quad (2)$$

at least for the survey smoothed near our upper wavenumber limit of $0.15 h \text{ Mpc}^{-1}$. In the CGC model, the redshift dependence of $b(L, z)$ is assumed to cancel that of the mass density field so that $\delta(L, \mathbf{r})$ is independent of redshift. Although galaxy bias has to be more complicated in detail, we may hope that there is a ‘linear response limit’ on large scales: those probed in the analysis presented in this paper. In the stochastic biasing framework proposed by Dekel & Lahav (1999), the simple model corresponds to a dimensionless galaxy–mass correlation coefficient $r_g = 1$. Wild et al. (2004) show that the correlation between $\delta(L, \mathbf{r})$ from different types of galaxies have $r_g > 0.95$.

Modelling the expansion of the density field in spherical harmonics and spherical Bessel functions is dependent on the linear redshift-space distortions parametrized by $\beta(L_*, z) \simeq \Omega_m(z)^{0.6}/b(L_*, z)$, a function of galaxy luminosity and epoch. The evolution of this parameter is dependent on that of the matter density $\Omega_m(z)$ and the galaxy bias $b(L_*, z)$. These effects are included in the method and are considered in Sections A1 and A4. The recovered expansion is

also dependent on the velocity dispersion σ_{pair} and model assumed for the Fingers of God effect (see Section 6.5).

We parametrize the shape of the power spectrum of L_* galaxies with the Hubble constant, h , in units of $100 \text{ km s}^{-1} \text{ Mpc}^{-1}$, the scalar spectral index n_s , and the matter density Ω_m through $\Omega_m h$ and the fraction of matter in baryons Ω_b/Ω_m . The contribution to the matter budget from neutrinos is denoted Ω_ν . The matter power spectrum is normalized using σ_8 , the present-day rms linear density contrast averaged over spheres of $8 h^{-1} \text{ Mpc}$ radius.

The shape of the power spectrum to current precision is only weakly dependent on h , and only sets a strong constraint on a combination of Ω_b/Ω_m , $\Omega_m h$, Ω_ν and n_s . In this paper, we only consider the very simple model of a constrained flat, scale-invariant adiabatic cosmology with Hubble parameter $h = 0.72$, and no significant neutrino contribution $\Omega_\nu = 0$. We show that this model is consistent with our analysis, as it is with recent CMB and LSS data sets (e.g. Spergel et al. 2003; Tegmark et al. 2003b). Additionally, we use Ω_b/Ω_m & $\Omega_m h$ to marginalize over the shape of the power spectrum when considering $\beta(L_*, 0)$ and $b(L_*, 0)\sigma_8$, and marginalize over $0 < \Omega_b/\Omega_m < 0.4$ and $0.1 < \Omega_m h < 0.4$. Given the precision to which the shape of the power spectrum can be constrained, there is an almost perfect degeneracy between Ω_b/Ω_m , $\Omega_m h$ and n_s . For $n_s \neq 1$, to the first order in n_s , our best-fitting values of Ω_b/Ω_m and $\Omega_m h$ would change by $0.46(n_s - 1)$ and $0.34(1 - n_s)$, respectively.

5.2 Results for the fixed power spectrum shape

In this section we fit $\beta(L_*, 0)$ and $b(L_*, 0)\sigma_8$ to the data assuming a concordance model power spectrum with $\Omega_m h = 0.21$, $\Omega_b/\Omega_m = 0.15$, $h = 0.72$ and $n_s = 1$, consistent with the recent *Wilkinson Microwave Anisotropy Probe* (WMAP) results (Spergel et al. 2003), and close to the true parameters of the Hubble Volume mocks. Likelihood contours for $b(L_*, 0)\sigma_8$ and $\beta(L_*, 0)$ are presented in Fig. 2 for the 2dFGRS and mock catalogues. The primary degeneracy between these parameters arises because $b(L_*, 0)\sigma_8$ is a measure of the total power, combining radial and angular modes. Increasing $\beta(L_*, 0)$ beyond the best-fitting value increases the power of the model radial modes, requiring a decrease in the overall power to approximately fit the data. In order to show that this degeneracy corresponds to models with the same redshift-space power spectrum amplitude, the dashed lines in Fig. 2 show the locus of models with the same redshift-space power spectrum amplitude as the maximum likelihood (ML) solution. Here, the redshift-space and real-space power spectra, represented by P_s and P_r , are assumed to be related by

$$P_s = \left(1 + \frac{2}{3}\beta + \frac{1}{5}\beta^2\right) P_r. \quad (3)$$

However, we still find tight constraints with $b(L_*, 0)\sigma_8 = 0.81 \pm 0.02$ and $\beta(L_*, 0) = 0.57 \pm 0.08$. In fact, in Section 5.3 we marginalize over a range of model power spectra shapes and show that these constraints are not significantly expanded when the shape of the power spectrum is allowed to vary.

5.3 Results without prior on the power spectrum shape

In Fig. 3 we present likelihood contours for $\Omega_m h$ and Ω_b/Ω_m assuming a Λ CDM power spectrum with fixed $n_s = 1.0$, and marginalizing over the power spectrum amplitude $b(L_*, 0)\sigma_8$ and $\beta(L_*, 0)$. Apart from the implicit dependence via $\Omega_m h$, there is virtually no residual sensitivity to h , so we set it at the Hubble key project value of $h = 0.72$ (Freedman et al. 2001). Contours are shown for the recovered likelihood calculated using the NGP and SGP catalogues

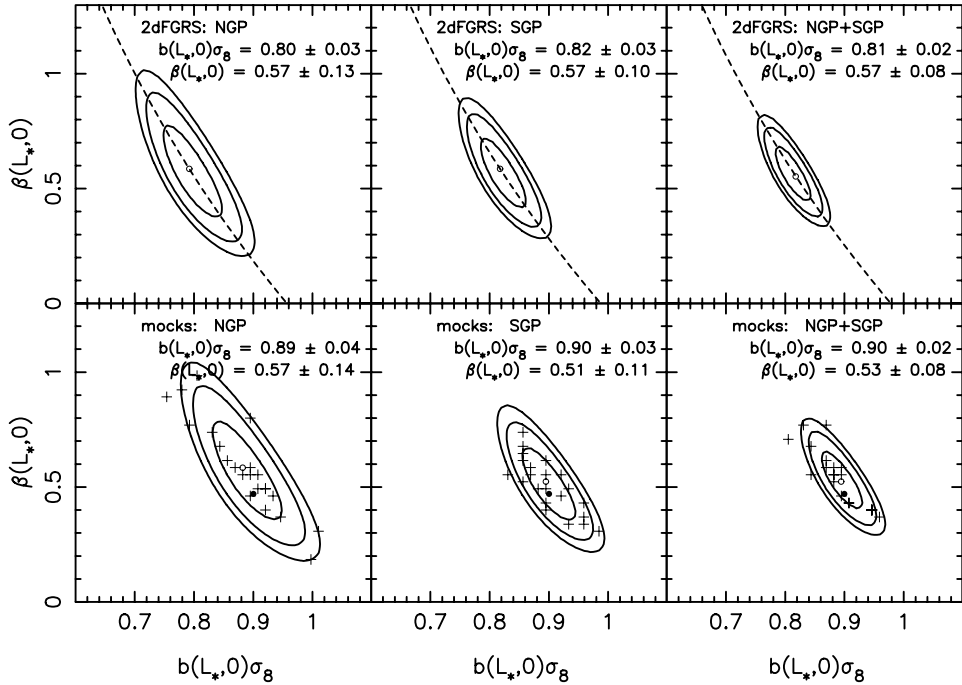


Figure 2. Likelihood contours for the recovered $b(L_*, 0)\sigma_8$ and $\beta(L_*, 0)$ assuming a fixed Λ CDM power spectrum shape. Solid lines in the top row show the recovered contours from the 2dFGRS, while the bottom row gives the average recovered contours from the Λ CDM mock catalogues. Contours correspond to changes in the likelihood from the maximum of $2\Delta \ln \mathcal{L} = 2.3, 6.0, 9.2$. These values correspond to the usual two-parameter confidence of 68, 95 and 99 per cent. The open circle marks the ML position, while the solid circle marks the true parameters for the mock catalogues. The crosses give the ML positions for the 22 mock catalogues. Note that on average 57 per cent of the crosses lie within the $2\Delta \ln \mathcal{L} = 2.3$ contour for the NGP and SGP mock catalogues. The chosen modes are not independent, although they are orthogonal, so we cannot assume that $\ln \mathcal{L}$ has a χ^2 distribution. See Section 5.4 for a further discussion of the confidence intervals that we place on recovered parameters. The dashed lines plotted in the upper panels give the locus of models with a constant redshift-space power spectrum amplitude (see text for details).

and from the combination of the two. We present the measured likelihood surface from the 2dFGRS catalogue and the average likelihood surface recovered from the mock catalogues. For both the 2dFGRS and the mocks, there is a broad degeneracy between $\Omega_m h$ and Ω_b/Ω_m , corresponding to models with a similar power spectrum shape. This degeneracy is partially lifted by the 2dFGRS data, with a low baryon fraction favoured. Fig. 4 shows a similar plot for $b(L_*, 0)\sigma_8$ and $\beta(L_*, 0)$, marginalizing over the power spectrum shape (parametrized by $\Omega_m h$ and Ω_b/Ω_m). Although this increases the size of the allowed region, the increase is relatively small, and we find $\beta(L_*, 0) = 0.58 \pm 0.08$ and $b(L_*, 0)\sigma_8 = 0.79 \pm 0.03$.

For the 2dFGRS catalogue, we present likelihood surfaces for all parameter combinations in our simple four-parameter model in Fig. 5. This plot shows that there is a degeneracy between $b(L_*, 0)\sigma_8$ and $\Omega_m h$ (as discussed for example in Lahav et al. 2002). However, $\beta(L_*, 0)$ appears to be independent of the power spectrum shape.

5.4 Confidence intervals for the parameters

Although the modes used are uncorrelated because of the KL data compression (Section A7), they are not independent, and we cannot assume that $\ln \mathcal{L}$ has a χ^2 distribution. However, we can still choose to set fixed contours in the likelihood as our confidence limits and simply need to test the amplitude of the contours to be chosen. Luckily, we have 22 mock catalogues from which we can estimate confidence intervals. For $b(L_*, 0)\sigma_8$ and $\beta(L_*, 0)$, with a fixed power spectrum, 57 per cent of the data points lie within the $2\Delta \ln \mathcal{L} = 2.3$ average contour for the NGP and SGP mock

catalogues. Marginalizing over the power spectrum shape leaves 54 per cent within the contour, 84 per cent with $2\Delta \ln \mathcal{L} < 6.0$ and 100 per cent with $2\Delta \ln \mathcal{L} < 9.2$. However, for power spectrum shape parameters $\Omega_m h$ and Ω_b/Ω_m , 77 per cent have $2\Delta \ln \mathcal{L} < 2.3$, all but one have $2\Delta \ln \mathcal{L} < 6.0$, and this mock has $2\Delta \ln \mathcal{L} < 9.2$.

Given the limited number of simulated catalogues, this is in satisfactory agreement. We note that the mocks were drawn from the Hubble Volume simulation (Evrard et al. 2002), and are consequently not completely independent. However, given that the numbers of mocks within the expected confidence intervals are close to those expected for independent Gaussian random variables, we feel justified in using the standard χ^2 intervals for our quoted parameters.

6 TESTS OF THE METHOD

In the Fourier-based analysis of P01 and C04, the expected variation in the measured power is only weakly dependent on the cosmological parameters and a fixed covariance matrix could therefore be assumed. In the analysis presented in this paper, the transformed density field is modelled rather than the power, and the likelihood variation due to cosmology is completely modelled using the covariance matrix – indeed, it is the variation of the covariance matrix that alters the likelihood and allows us to estimate the cosmological parameters. Consequently, we need to perform an inversion of this matrix for each cosmological model to be tested (an N^3 operation). For a fixed power spectrum shape, the variation in the inverse covariance matrix with $b(L_*, 0)\sigma_8$ and $\beta(L_*, 0)$ is small and we

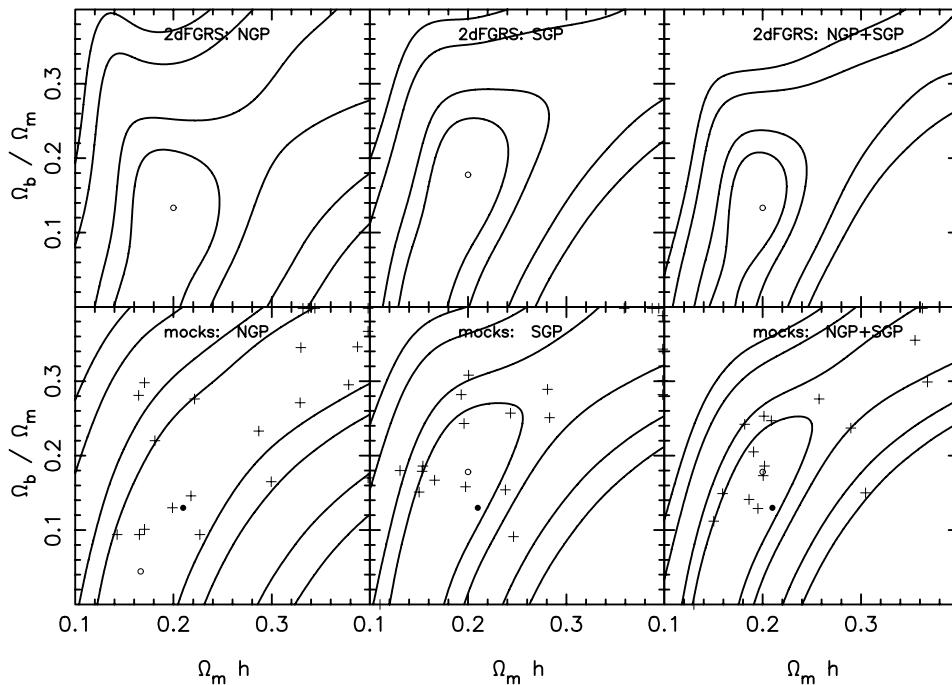


Figure 3. Likelihood contours for $\Omega_m h$ and Ω_b/Ω_m assuming a Λ CDM power spectrum with $h = 0.72$ and $n_s = 1.0$. We have marginalized over the power spectrum amplitude and $\beta(L_*, 0)$. The solid lines in the top row show the recovered contours from the 2dFGRS, while the bottom row gives the average recovered contours from the Λ CDM mock catalogues. The contours correspond to changes in the likelihood from the maximum of $2\Delta \ln L = 1.0, 2.3, 6.0, 9.2$. In addition to the contours plotted in Fig. 2, we also show the standard one-parameter 68 per cent confidence region to match with fig. 5 in P01. The open circle marks the ML position. As in P01, we find a broad degeneracy in the $(\Omega_m h, \Omega_b/\Omega_m)$ plane, which is weakly lifted with a low baryon fraction favoured for the 2dFGRS data. These parameter constraints are less accurate than those derived in C04 as we use less data, and we limit the number of modes used. The ML positions for the 22 mock catalogues are shown by the crosses. It can be seen that a number of the mock catalogues have likelihood surfaces that are not closed, with the ML position being at one edge of the parameter space considered. However, these mocks all follow the general degeneracy between models with the same $P(k)$ shape.

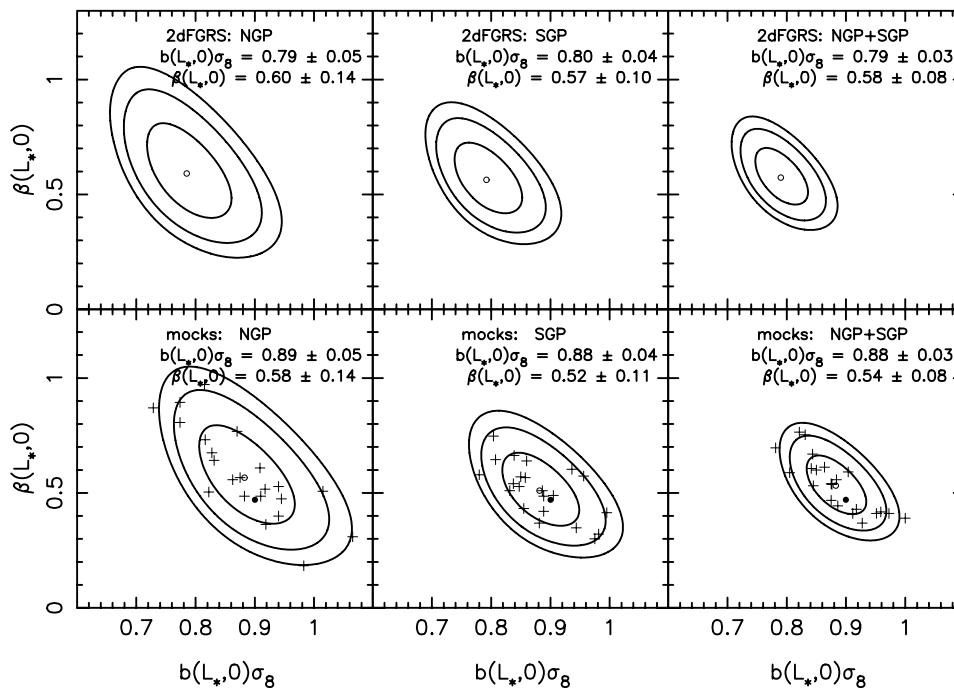


Figure 4. As for Fig. 2, but now marginalizing over the power spectrum shape as parametrized by $\Omega_m h$ and Ω_b/Ω_m . As can be seen, allowing for different power spectrum shapes only increases the errors on $b(L_*, 0)\sigma_8$ and $\beta(L_*, 0)$ slightly. The relative interdependence between the power spectrum shape and $b(L_*, 0)\sigma_8$ and $\beta(L_*, 0)$ is considered in more detail in Fig. 5.

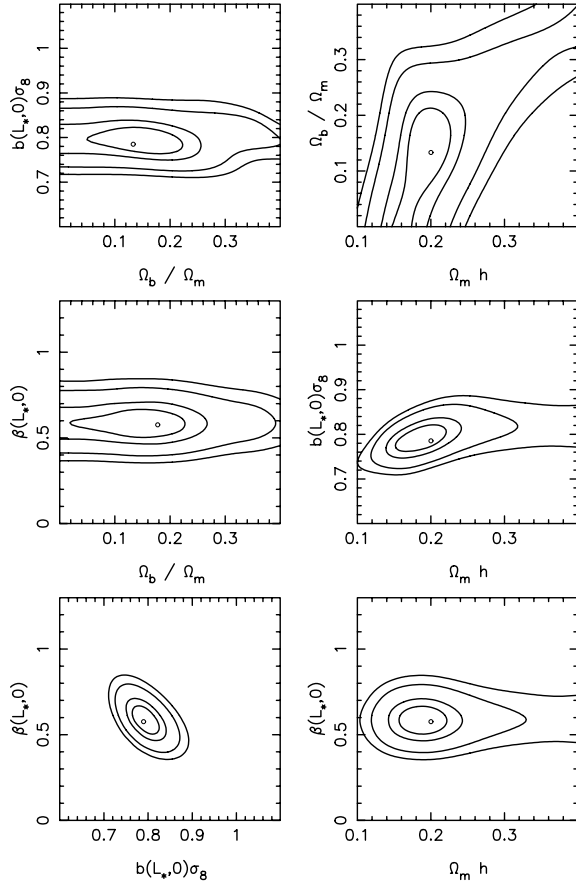


Figure 5. Contour plots showing changes in the likelihood from the maximum of $2\Delta \ln L = 1.0, 2.3, 6.0, 9.2$ for different parameter combinations for the combined likelihood from the 2dFGRS NGP and SGP catalogues, assuming a Λ CDM power spectrum with $h = 0.72$ and $n_s = 1.0$. There are four parameters in total, and in each plot we marginalize over the two other parameters. The primary degeneracy arises between $\Omega_m h$ and Ω_b / Ω_m , and corresponds to similar power spectrum shapes. $b(L_*, 0)\sigma_8$ is also degenerate with $\Omega_m h$, although $\beta(L_*, 0)$ is independent of the power spectrum shape.

can use an iterative trick (described in Section A8) to estimate the covariance matrix using an N^2 operation. The covariance matrix obviously varies more significantly when we allow the cosmological parameters to vary more freely and the shape of the power spectrum changes. A full matrix inversion is then required for each model tested. This is computationally intensive and consequently the specific tests presented in this section are based around recovering $b(L_*, 0)\sigma_8$ and $\beta(L_*, 0)$ for a fixed $P(k)$ shape.

In Figs 6 and 7 we present recovered likelihood surfaces calculated with various changes to our method. These plots demonstrate tests of our basic assumptions and of our implementation of the spherical harmonics method.

6.1 Mock catalogues

In addition to the 2dFGRS results presented in Figs 2–4, we also plot contours revealing the average likelihood surface determined from the 22 mock catalogues described in Section 3. The average surface is used so the 2dFGRS and mock contours are directly comparable. For $b(L_*, 0)\sigma_8$ and $\beta(L_*, 0)$ we also give the recovered parameters and errors from the average likelihood surface. These numbers can be compared with the expected values $b(L_*, 0)\sigma_8 =$

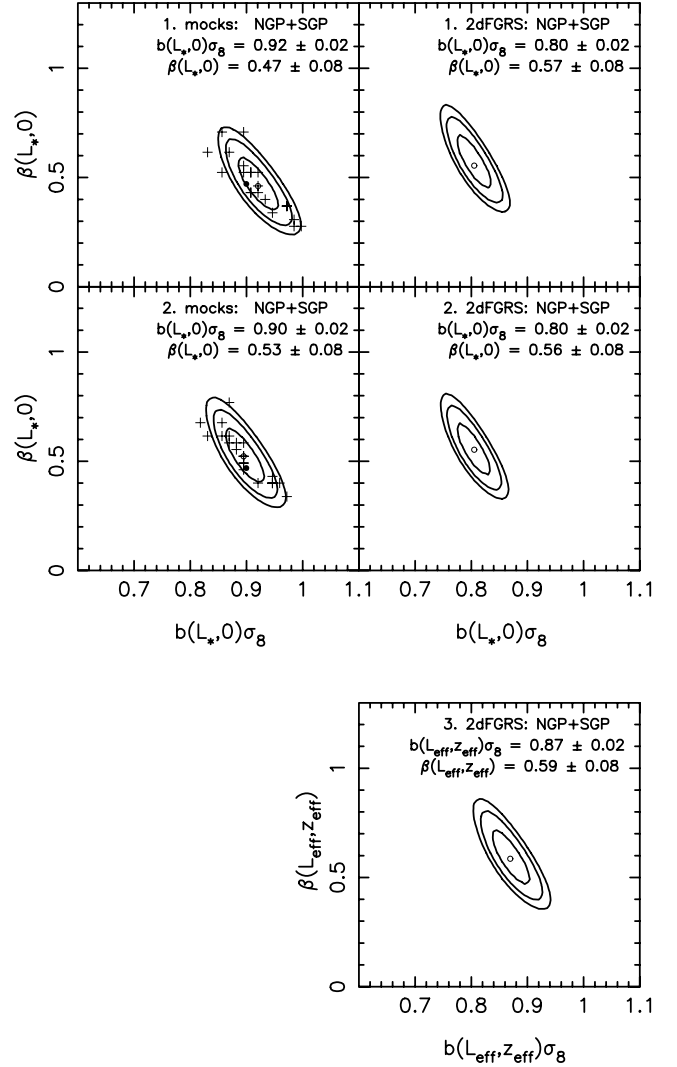


Figure 6. Likelihood contour plots as in Fig. 2, but now designed to test the spherical harmonics method. The different rows correspond to models with: (1) power spectrum shape corresponding to the linear rather than the non-linear model; (2) 1/completeness weighting for galaxies so that the weighted angular mask is uniform over the area of the survey; and (3) no luminosity bias correction.

0.9 and $\beta(L_*, 0) = 0.47$. Crosses in these plots show the ML positions calculated from each of the mock catalogues, while the open circle gives the combined ML position, and the solid circles show the expected values. We see that the recovered value of $\beta(L_*, 0)$ is slightly higher than expected. However, we will show in Section 6.7 that the recovered value of $\beta(L_*, 0)$ changes in a consistent way following changes in the peculiar velocities calculated for the galaxies in each mock. Furthermore, we show that there is no evidence for a systematic offset in the recovered $\beta(L_*, 0)$, which we would expect to vary with the peculiar velocities. The true value of $b(L_*, 0)\sigma_8$ is recovered to sufficient precision.

6.2 Non-linear power assumption

Although the width of the window function means that the modes are dependent on the real-space power spectrum at $k > 0.2 h \text{ Mpc}^{-1}$, this dependence is weak compared with the dependence on the low- k , linear regime (this is shown in Fig. A1). The likelihood calculation

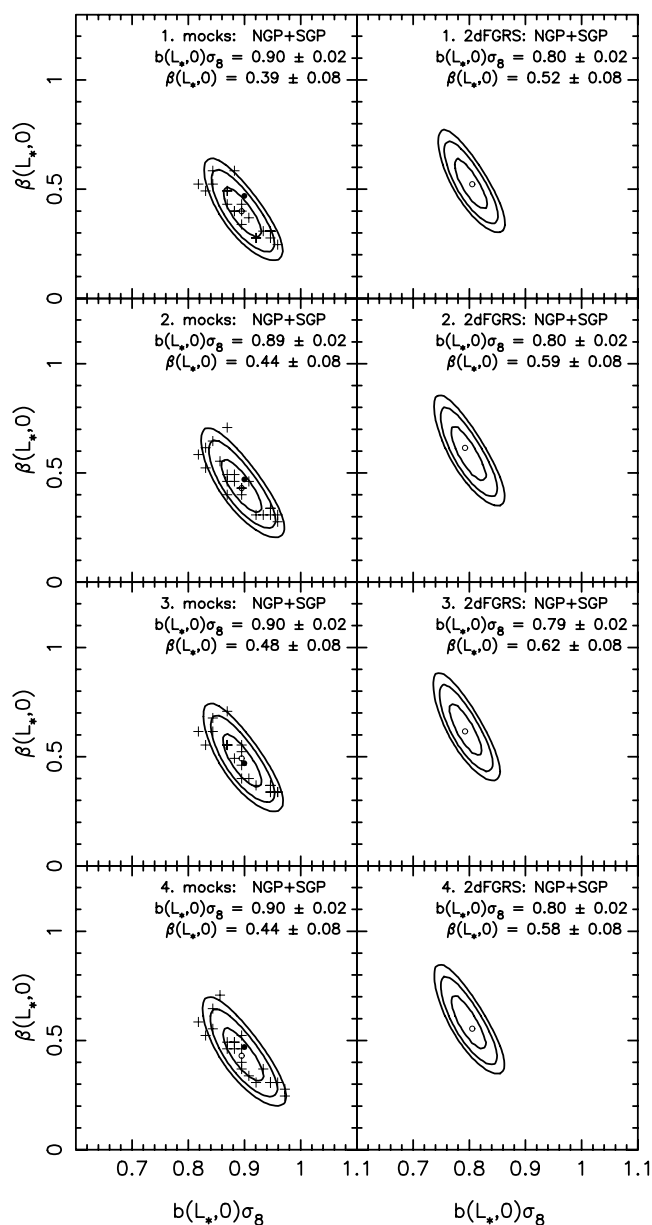


Figure 7. Likelihood contour plots as in Fig. 2, but now designed to test the effect of the Fingers of God correction applied. The different rows correspond to models with: (1) no Fingers of God correction applied; (2) an exponential model for the probability distribution caused by the Fingers of God effect (equation 5) with $\sigma_{\text{pair}} = 400 \text{ km s}^{-1}$; (3) a Gaussian model the probability distribution (equation 6) with $\sigma_{\text{pair}} = 400 \text{ km s}^{-1}$; and (4) a model with an exponential distribution for the correlation function (equation 7) with $\sigma_{\text{pair}} = 400 \text{ km s}^{-1}$.

used in equation (A43) relied on the transformed density field having Gaussian statistics. While this is expected to be true in the linear regime, on the scales of non-linear collapse this assumption must break down. Although the modes must deviate from Gaussianity, we consider the change in shape of the power as a first approximation, and use the fitting formulae of Smith et al. (2003) to determine the model power. In order to test the significance of this, we consider the effect of replacing the non-linear power in the model (equation A40) with the linear power. In fact, this has a relatively small effect on the recovered power spectrum amplitude and $\beta(L_*, 0)$ as shown in Fig. 6.

6.3 Completeness weighting

We have tried two angular weighting schemes for the galaxies. The default weights do not have an angular component, and are simply the radial weights of Feldman et al. (1994) given by equation (A5). For comparison we have also tried additionally weighting each galaxy by $1/(\text{angular completeness})$, so the weighted galaxy density field at a given r is independent of angular position (i.e. it is uniform over the survey area). This weighting simplifies the convolution of the model power to correct for the angular geometry of the survey (equation A22 and A27), and comparing results from both schemes therefore tests this convolution. The downside of such a weighting is the slight increase in shot noise. Results calculated with this weighting scheme are presented in Fig. 6, and can be compared with the default in Fig. 2: no significant difference is observed between the two schemes.

6.4 Luminosity-dependent bias

As described in Section A1, we adopt a CGC model for the evolution of the fluctuation amplitudes across the survey, and correct for the expected luminosity dependence of this amplitude by weighting each galaxy by the reciprocal of the expected bias ratio to L_* galaxies (as suggested by Percival et al. 2004). The expected bias ratio assumed, given by equation (A1), was calculated from a volume-limited subsample of the 2dFGRS by Norberg et al. (2001). In Fig. 6, we fit models that do not include either this luminosity-dependent bias correction, or the evolution correction for $\beta(L, z)$. This likelihood fit measures $\beta(L_{\text{eff}}, z_{\text{eff}})$, which is now a function of the effective luminosity L_{eff} and effective redshift z_{eff} of the survey. For the complete survey, examining the weighted density field gives that $L_{\text{eff}} = 1.9L_*$ and $z_{\text{eff}} = 0.17$. However, we cannot be sure that the spherical harmonics modes selected will not change these numbers.

In fact, fitting to the data gives $\beta(L_{\text{eff}}, z_{\text{eff}}) = 0.59 \pm 0.08$ and $b(L_{\text{eff}}, z_{\text{eff}})\sigma_8(z_{\text{eff}}) = 0.87 \pm 0.02$. In order to compare these values with our results that have been corrected for luminosity-dependent bias, we have to consider a number of factors. For the CGC model, the change in the measured power spectrum amplitude should only arise from the galaxy luminosity probed. The effective luminosity of the sample is $\sim 1.9L_*$, which gives an expected bias of 1.13 (using equation A1). The observed offset in amplitude is 1.08, perhaps indicating that, for the chosen modes, $L_{\text{eff}} < 1.9L_*$. Within the CGC model, $\beta(L_{\text{eff}}, z_{\text{eff}})$ is expected to be related to $\beta(L_*, 0)$ by

$$\beta(L_{\text{eff}}, z_{\text{eff}}) = \frac{\Omega_m(z_{\text{eff}})^{0.6}}{\Omega_m(0)^{0.6}} D(z_{\text{eff}}) \frac{b(L_*, 0)}{b(L_{\text{eff}}, 0)} \beta(L_*, 0), \quad (4)$$

which gives $\beta(1.9L_*, 0.17) \sim \beta(L_*, 0)$ for a concordance cosmological model as the different factors approximately cancel. In fact, we measure no significant difference between $\beta(L_{\text{eff}}, z_{\text{eff}})$ and $\beta(L_*, 0)$.

6.5 Fingers of God correction

In this section we test the assumed scattering probability that corrects distance errors induced by the peculiar velocities of galaxies inside groups. This probability was used to convolve the model transformed density fields using the matrix presented in equation (A10). We compare models with exponential and Gaussian forms, and a model that corresponds to an exponential convolution for the correlation function (this corresponds to the model advocated by

Ballinger, Peacock & Heavens 1996; Hawkins et al. 2003)

$$p_c(r - y) = \frac{1}{\sqrt{2}\sigma_v} \exp\left(-\frac{\sqrt{2}|r - y|}{\sigma_v}\right), \quad (5)$$

$$p_g(r - y) = \frac{1}{\sqrt{2\pi}\sigma_v} \exp\left[-\frac{(r - y)^2}{2\sigma_v^2}\right], \quad (6)$$

$$p_b(r - y) = \frac{2\sqrt{2}}{\sigma_v} K_0\left[-\frac{\sqrt{2}}{\sigma_v}(r - y)\right]. \quad (7)$$

σ_v is the one-dimensional velocity dispersion, related to the commonly used pairwise velocity dispersion by $\sigma_{\text{pair}} = \sqrt{2}\sigma_v$. K_n is an n th-order modified Bessel function derived as the inverse Fourier transform of the root of a Lorentzian (Taylor et al. 2001).

The Fingers of God effect stretches structure along the line of sight, whereas large-scale bulk motions tend to foreshorten objects. Although these effects predominantly occur on different scales, there is some overlap, and if the Fingers of God effect is not included when modelling the data, the best-fitting value of $\beta(L_*, 0)$ is decreased slightly. In this case, the best-fitting model interpolates between the two effects, as demonstrated in Fig. 7, where we present the best-fitting $\beta(L_*, 0)$ with and without the Fingers of God correction.

In the results presented in Fig. 2, we assumed an exponential distribution for the distribution function of random motions with $\sigma_{\text{pair}} = 350 \text{ km s}^{-1}$ for the 2dFGRS catalogue and $\sigma_{\text{pair}} = 500 \text{ km s}^{-1}$ for the mock catalogues. We have tried a number of different values of $0 < \sigma_{\text{pair}} < 500 \text{ km s}^{-1}$ and find only very small variation in the best-fitting $\beta(L_*, 0)$, as expected because we have chosen modes that peak for $k < 0.15 h \text{ Mpc}^{-1}$, where the Fingers of God correction is small. To demonstrate this, in Fig. 7 we present results calculated using equations (5)–(7) with $\sigma_{\text{pair}} = 400 \text{ km s}^{-1}$ for both the 2dFGRS and the mock catalogues. We also compare with the effect of not including any correction for the small-scale velocity dispersion. Little difference is seen in the recovered values of $\beta(L_*, 0)$, adding weight to the hypothesis that the Fingers of God correction is unimportant in our determination of $\beta(L_*, 0)$.

In the $\xi(\sigma, \pi)$ analyses of the 2dFGRS presented in Peacock et al. (2001), Madgwick et al. (2003) and Hawkins et al. (2003) a strong degeneracy was revealed between the Fingers of God and linear redshift-space distortions. Although such a degeneracy is also present in the results from our spherical harmonics analysis, it is weak compared with the $\xi(\sigma, \pi)$ results. The difference is due to the scales analysed – the correlation function studies estimated the clustering strength on smaller scales where the Fingers of God convolution is more important. As the Fingers of God effect has less effect in our analysis, we are less able to constrain its amplitude, and therefore assume a fixed value motivated by the $\xi(\sigma, \pi)$ analyses, rather than fitting to the data.

6.6 2dFGRS catalogue calibration

In this section we consider the 2dFGRS release catalogue and corresponding calibration. In order to test the dependence of our results on the catalogue calibration, in this section we report on the analysis of a different version of the catalogue with revised calibration. In the release catalogue (Colless et al. 2003; <http://www.mso.anu.edu.au/2dFGRS/>) the 2dFGRS photographic magnitudes were calibrated using external CCD data from the SDSS Early Data Release and European Southern Observatory Imaging Survey (EIS) (Colless et al. 2003; Cross et al. 2003). Overlaps between the photographic plates allow this calibration to be propa-

gated to the whole survey. In this section we instead calibrate each plate without the use of external data. The magnitudes in the final released catalogue, b_J^{final} and magnitudes, b_J^{self} , resulting from this self-calibration are assumed to be related by a linear relation

$$b_J^{\text{self}} = a_{\text{self}} b_J^{\text{final}} + b_{\text{self}}, \quad (8)$$

where the calibration coefficients a_{self} and b_{self} are allowed to vary from plate to plate. To set the values of these calibration coefficients two constraints are applied. First on each plate we assume that the galaxy luminosity function can be represented by a Schechter function with faint-end slope $\alpha = 1.2$ and make a ML estimate of M_* . The value of M_* is sensitive to the difference in b_J^{self} and b_J^{final} at around $b_J = 17.5$ and the number of galaxies on each plate is such that the typical random error on M_* is 0.03 magnitudes. Secondly, we compare the number of galaxies, $N(z > 0.25)$, with redshifts greater than $z = 0.25$ with the number we expect, $N_{\text{model}}(z > 0.25)$, based on our standard model of the survey selection function. The value of $N_{\text{model}}(z > 0.25)$ depends sensitively on the survey magnitude limit and so constrains the difference in b_J^{self} and b_J^{final} at $b_J \approx 19.5$. By demanding that on each plate both $N(z > 0.25) = N_{\text{model}}(z > 0.25)$ and $M_* - 5 \log h = 19.73$ we determine a_{self} and b_{self} . This method of calibrating the catalogue is extreme in that it ignores the CCD calibrating data (apart from setting the overall zero point of $M_* - 5 \log h = 19.73$). A more conservative approach is to combine the external calibration with the internal one and determine a_{self} and b_{self} by a χ^2 procedure that takes account of the statistical error on M_* , the expected variance on $N(z > 0.25)$ given by mock catalogues and the errors on the calibrating data. Unless the errors on the CCD calibration are artificially inflated this results in a calibration very close to that of final release. Thus we believe that the difference between the results achieved with the self-calibrated catalogue and the standard final catalogue represent an upper limit on the effects attributable to uncertainty in the photometric calibration.

For the spherical harmonics analysis method, we need to cut the 2dFGRS catalogue so that the radial distribution of galaxies is independent of angular position (this catalogue reduction was described in Section 2). Changing the magnitude limit at which to cut the catalogue changes the angular mask for the reduced sample as angular regions that do not go as faint as the chosen limit are removed. Rather than optimize the magnitude limit at which to cut the self-calibrated catalogue, we instead resample the revised catalogue using the old mask. A magnitude limit was then chosen to fully sample this angular region and give a radial distribution that is independent of angular position. This procedure avoided the computationally expensive recalculation of angular matrices (see Appendix A). However, the radial galaxy distribution and total number of galaxies were different from those in our primary analysis, and a revised radial component of the covariance matrix was required.

Revised parameter constraints on $\beta(L_*, 0)$ and $b(L_*, 0)\sigma_8$ are presented in Fig. 8, which can be directly compared with the upper panels in Fig. 2. An incorrect calibration would lead to a resampling of the complete 2dFGRS catalogue (described in Section 2) that would not produce a catalogue with radial galaxy distribution independent of angular position. This would lead to an increase in the amplitude of the observed angular fluctuations. Given that we split the fluctuations into an overall power spectrum and an additional component in the radial direction caused by linear redshift-space distortions, an artificial increase in angular clustering would manifest itself as an increase in $b(L_*, 0)\sigma_8$, coupled with a decrease in $\beta(L_*, 0)b(L_*, 0)\sigma_8$, which controls the absolute amplitude of the linear redshift-space distortions. In fact this is exactly what is observed when comparing results from the release and self-calibration

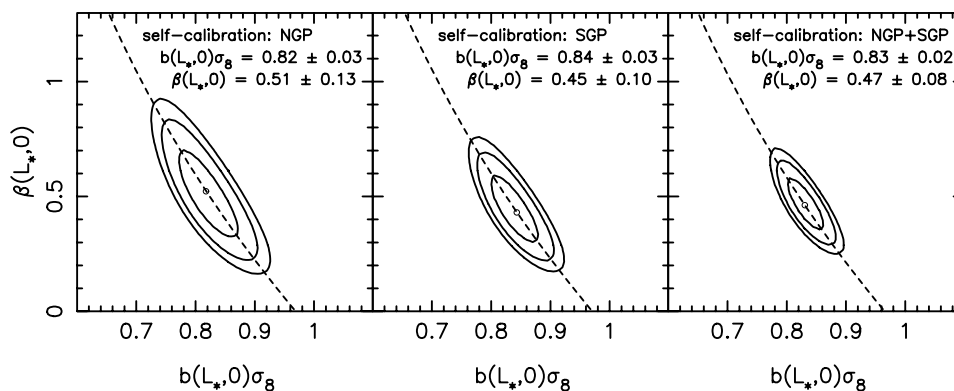


Figure 8. Likelihood contours for the recovered $b(L_*, 0)\sigma_8$ and $\beta(L_*, 0)$ assuming a fixed Λ CDM power spectrum shape as in Fig. 2, but now calculated having revised the calibration of the 2dFGRS catalogue. Details of the revised calibration are presented in Section 6.6.

catalogues (Figs 2 and 8), suggesting that the self-calibration procedure introduces artificial angular distortions into the reduced catalogue. The dashed lines in Fig. 8 show the locus of models with redshift-space power spectrum amplitude (calculated from equation 3) at the ML value. Comparing the relative positions of the ML points in Figs 2 and 8 shows that changing the catalogue calibration moves the ML position along this locus, without significantly changing the redshift-space power amplitude. Catalogue calibration and selection represents the most significant potential source of systematic error in our analysis.

6.7 Testing $\beta(L_*, 0)$ using mock catalogues

For each galaxy in the mock catalogues, we know the relative contributions to the redshift from the Hubble flow and peculiar velocity. Consequently, we can easily increase or decrease the amplitude of the redshift-space distortions to mimic catalogues with different cosmological parameters. In Fig. 9 we plot the recovered power spectrum amplitudes and $\beta(L_*, 0)$ from catalogues created by increasing or decreasing the peculiar velocity by 50 per cent from the true value. Obviously, this changes both the linear redshift-space distortions and the Fingers of God, and consequently we fit to these data assuming a revised σ_{pair} value. If we did not do this, the average recovered $\beta(L_*, 0)$ value would vary from the true value by less than 50 per cent, as assuming the wrong value of σ_{pair} has the effect of damping the change in the recovered $\beta(L_*, 0)$. However, because the linear redshift-space distortions are dominant on the scales being probed in our analysis, we would still see a change in the correct direction. For these catalogues, we find that altering the peculiar velocities results in a consistent change in the recovered $\beta(L_*, 0)$, showing that our likelihood test is working well.

In Fig. 9 we also show the recovered parameter constraints from mocks catalogues with no redshift-space distortions. Here, we fitted to these data assuming that there was no Fingers of God effect, and see that we recover for $\beta(L_*, 0)$ consistent with zero for each catalogue.

7 SUMMARY AND DISCUSSION

The spherical harmonics analysis method of HT and Tadros et al. (1999) has been extended and updated to allow for surveys that cover a relatively small fraction of the sky. Additionally, a consistent approach has been adopted to model luminosity-dependent bias and the evolution of the matter power spectrum. We assume a CGC

model for the redshift region $0 < z < 0.25$ covered by the 2dFGRS survey, in which, although the matter density field does evolve, the galaxy power spectrum is assumed to remain fixed. Galaxy bias is also assumed to be a function of luminosity, and we correct for the effect that this has on the recovered power spectrum.

The revised method has been applied to the complete 2dFGRS catalogue, resulting in tight constraints on the amplitude of the linear redshift-space distortions. As the method still requires a survey with selection function separable in radial and angular directions, we have to use a reduced version of the final 2dFGRS catalogue. Additionally, we are forced to compromise on the quantity of data (number of modes) analysed, although we have tried to perform a logical and optimized reduction of the mode number. These considerations mean that we do not obtain the accuracy of the cosmological constraints from the shape of the galaxy power spectrum obtained in our companion Fourier analysis (C04). This reduction in accuracy primarily results from the decrease in the catalogue size. In particular, the analysis is cosmic variance limited and most of the discarded galaxies were luminous and therefore at high redshift where they trace a large volume of the Universe. However, from the spherical harmonics method we do obtain power spectrum shape constraints $\Omega_b/\Omega_m < 0.21$ as shown in Fig. 3 and, for fixed $\Omega_b/\Omega_m = 0.17$, we find $\Omega_m h = 0.20^{+0.03}_{-0.03}$, consistent with previous power spectrum analyses from the 2dFGRS and the SDSS.

We have also modelled the overdensity distribution in 22 LCDM mock catalogues, designed to mimic the 2dFGRS. By presenting recovered parameters from these catalogues, we have shown that any systematic biases induced by the analysis method are at a level well below the cosmic variance caused by the size of the survey volume. In particular, it should be emphasized that these mocks include a realistic degree of scale-dependent bias, to reflect the known difference in small-scale clustering between galaxies and the non-linear CDM distribution (e.g. Jenkins et al. 1998). We have additionally used these catalogues to test the errors placed on recovered parameters and find that assuming a χ^2 distribution for $\ln \mathcal{L}$ provides approximately the correct errors. The tests presented, considering the NGP and SGP separately, using the mocks and varying parts the analysis method were designed to test our spherical harmonics formalism and the assumptions that go into this. In particular, we do not test the 2dFGRS sample for internal consistency, for instance splitting by redshift or magnitude limit, although we do find consistent parameter estimates from the northern and southern parts of the survey. A more comprehensive set of tests is presented in C04, using Fourier methods to decompose the density field.

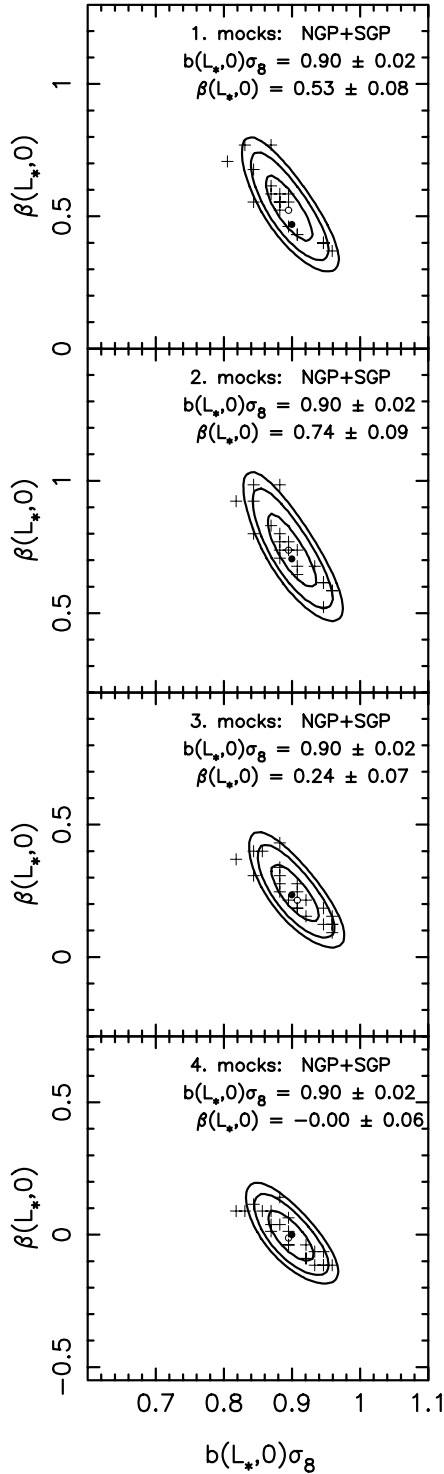


Figure 9. Likelihood contour plots as in Fig. 2, but now designed to test our recovery of $\beta(L_*, 0)$ using the mock catalogues. The different panels correspond to the following. (1) the standard catalogues with peculiar velocities calculated directly from the Hubble Volume simulation. Here the true value of $\beta(L_*, 0)$ is 0.47. (2) The contribution to the galaxy redshifts from the peculiar velocities has been increased by 50 per cent. Here, we assume $\sigma_{\text{pair}} = 750 \text{ km s}^{-1}$. Without this correction, $\beta(L_*, 0)$ would increase by less than 50 per cent. We expect $\beta(L_*, 0) = 0.71$, shown by the solid circle. (3) As (2), but now decreasing the redshift contribution by 50 per cent. $\sigma_{\text{pair}} = 250 \text{ km s}^{-1}$ is assumed, and we expect $\beta(L_*, 0) = 0.24$. (4) Recovered parameters from real-space catalogues, calculated assuming that $\sigma_{\text{pair}} = 0$. Obviously, we expect to recover $\beta(L_*, 0) = 0.0$.

By considering a revised 2dFGRS catalogue calibration, we have examined the effect of small systematic magnitude errors on our analysis. Such errors artificially increase the strength of the angular clustering, leading to an increase in the best-fitting $b(L_*, 0)\sigma_8$ and a corresponding decrease in $\beta(L_*, 0)$. We have shown that the revised catalogue tested produces such a change in the recovered parameters, therefore providing evidence in favour of the release calibration. The calibration method and its effect will be further discussed in C04. Here, we simply note that the systematic error in $\beta(L_*, 0)$ and $b(L_*, 0)$ from catalogue calibration is of the same order as the random error.

The strength of the spherical harmonics method as applied to the 2dFGRS lies in measuring the linear redshift-space distortions, and fitting the real-space power spectrum amplitude. Consequently we are able to measure $\beta(L_*, 0) = 0.58 \pm 0.08$, and $b(L_*, 0)\sigma_8 = 0.79 \pm 0.03$ for L_* galaxies at $z = 0$, marginalizing over the power spectrum shape. This result is dependent on the CGC model and on the bias-luminosity relationship derived by Norberg et al. (2001), and covers $0.02 < k < 0.15 h \text{ Mpc}^{-1}$. Our measurement of $\beta(L_*, 0)$ is derived on larger scales than the $\xi(\sigma, \pi)$ analyses of the 2dFGRS presented in Peacock et al. (2001) and Hawkins et al. (2003), and scale-dependent bias could therefore explain why our result is slightly higher than the numbers obtained in these analyses.

Tegmark et al. (2002) performed a similar spherical harmonics analysis of the 100-k release of the 2dFGRS. As in the analysis presented here, they also required a catalogue that was separable in radial and angular directions, and cut the 100-k release catalogue to 66 050 galaxies. From these galaxies, they measured $\beta(L_{\text{eff}}, z_{\text{eff}}) = 0.49 \pm 0.16$, consistent with our result (see Section 6.4 for a discussion of the conversion between $\beta(L_{\text{eff}}, z_{\text{eff}})$ and $\beta(L_*, 0)$). Our result not only allows for luminosity-dependent bias and evolution, it also uses over twice as many galaxies as the Tegmark et al. (2002) analysis.

On large scales, galaxies are expected to directly trace the bulk motion of the density field, so the absolute amplitude of the observed redshift-space distortions caused by this motion is expected to be independent of galaxy properties. This assumption has been tested empirically by considering the mean relative velocity of galaxy pairs in different samples (Juszkiewicz et al. 2000; Feldman et al. 2003). Rather than fitting $\beta(L_*, 0)$, the relative importance of the linear redshift-space distortions compared with the real-space galaxy power spectrum, we can instead fit the absolute amplitude of these fluctuations. This results in the cosmological constraint $\Omega_m^{0.6}\sigma_8 = 0.46 \pm 0.06$.

The relatively high power of σ_8 compared to Ω_m in this constraint means that an additional constraint on Ω_m provides a tight constraint on σ_8 . For example, fixing $\Omega_m = 0.3$ gives $\sigma_8 = 0.95 \pm 0.12$ (~ 15 per cent error), while fixing $\sigma_8 = 0.95$ gives $\Omega_m = 0.3 \pm 0.08$ (~ 26 per cent error). We note that our constraint is approximately 1σ higher than a recent combination of weak-lensing measurements that gave $\sigma_8 \simeq 0.83 \pm 0.04$ for $\Omega_m = 0.3$ (Refregier 2003). Additionally, combining the weak-lensing constraint with our measurement of $b(L_*, 0)\sigma_8$ suggests that $b(L_*, 0) \sim 0.9$ in agreement with the analyses of Lahav et al. (2002) and Verde et al. (2002). Similarly, combining our measurement of $\beta(L_*, 0)$ with recent constraints on Ω_m (such as those derived by Spergel et al. 2003) suggests that $b(L_*, 0) \sim 0.9$, and we see that we have a consistent picture of both the amplitude of the real-space power spectrum and the linear redshift-space distortions within the concordance Λ CDM model.

A comparison of our results with parameter constraints from *WMAP* is presented in Fig. 10. In this paper, we do not attempt to perform a full likelihood search for the best-fitting cosmological

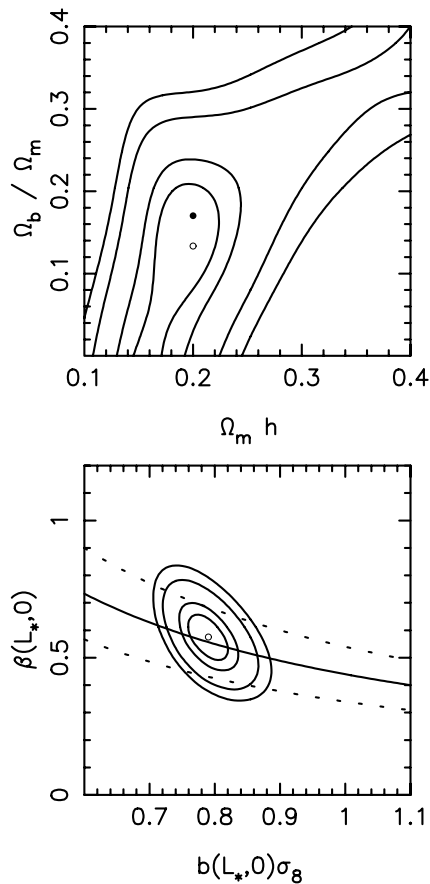


Figure 10. Likelihood contour plots for the combined NGP +SGP 2dFGRS catalogue as in Fig. 5 compared with best-fitting parameters from *WMAP* (Bennett et al. 2003; Spergel et al. 2003). The constraint on the characteristic amplitude of velocity fluctuations from the 1-year *WMAP* data is $\sigma_8 \Omega_m^{0.6} = 0.44 \pm 0.10$, which is shown in the left panel by the thick solid line, with 1σ errors given by the dotted lines. In the right panel, the solid circle shows the best-fitting parameter values of $\Omega_m h = 0.20$ and $\Omega_b / \Omega_m = 0.17$. As can be seen, the constraints resulting from the 2dFGRS power spectrum shape and the linear distortions are consistent with the *WMAP* data.

model using the combined 2dFGRS and *WMAP* data sets. Instead, we simply consider the consistency between the *WMAP* data and our measurements of the 2dFGRS. In Fig. 10 we plot the *WMAP* constraint on $\Omega_m^{0.6} \sigma_8$ as derived in Spergel et al. (2003), compared with our constraints on $\beta(L_*, 0)$ and $b(L_*, 0) \sigma_8$. *WMAP* obviously tells us nothing about $b(L_*, 0)$, so there is a perfect degeneracy between these parameters. However, the constraints are seen to be consistent. In fact our constraint is a significant improvement on the *WMAP* constraint, primarily because of the uncertainty in the optical depth to the last scattering surface, parametrized by τ .

As $h = 0.72$ is fixed in the simple cosmological model assumed to parametrize the power spectrum shape, the horizon angle degeneracy for flat cosmological models (Percival et al. 2002; Page et al. 2003) is automatically lifted. The position of the first peak in the CMB power spectrum therefore provides a tight constraint on Ω_m . In fact, given this simple model, the constraints on Ω_m and Ω_b / Ω_m from *WMAP* are so tight that we chose to plot a point to show them in Fig. 10, rather than a confidence region. However, had we considered a larger set of models in which h was allowed to vary, then an extra constraint is required to break the horizon angle degeneracy even for the *WMAP* data (Page et al. 2003). In this paper we

provide a new cosmological constraint by measuring the strength of the linear distortions caused by the bulk flow of the density field mapped by the final 2dFGRS catalogue.

ACKNOWLEDGMENTS

The 2dFGRS was made possible through the dedicated efforts of the staff of the Anglo-Australian Observatory, both in creating the 2dF instrument and in supporting it on the telescope. WJP is supported by PPARC through a Postdoctoral Fellowship. JAP and OL are grateful for the support of PPARC Senior Research Fellowships.

REFERENCES

- Abazajian K. et al., 2004, *AJ*, 128, 502
 Ballinger W. E., Heavens A. F., Taylor A. N., 1995, *MNRAS*, 276, L59
 Ballinger W. E., Peacock J. A., Heavens A. F., 1996, *MNRAS*, 282, 877
 Bennett C. L. et al., (The *WMAP* Team), 2003, *ApJS*, 148, 1
 Berlind A. A., Narayanan V. K., Weinberg D. H., 2001, *ApJ*, 549, 688
 Cole S., Fisher K. B., Weinberg D. H., 1995, *MNRAS*, 275, 515
 Cole S., Hatton S., Weinberg D. H., Frenk C. S., 1998, *MNRAS*, 300, 945
 Colless M. et al., 2001, *MNRAS*, 328, 1039
 Colless M. et al., 2003, preprint (astro-ph/0306581)
 Courteau S., van den Bergh S., 1999, *AJ*, 118, 337
 Cross N. J. G., Driver S. P., Liske J., Lemon D. J., Peacock J. A., Cole S., Norberg P., Sutherland W. J., 2003, *MNRAS*, 349, 576
 Dekel A., Lahav O., 1999, *ApJ*, 520, 24
 Efstathiou G. et al., (The 2dFGRS Team), 2002, *MNRAS*, 330, 29
 Eisenstein D. J., Hu W., 1998, *ApJ*, 496, 605
 Evrard A. E. et al., 2002, *ApJ*, 573, 7
 Feldman H. A., Kaiser N., Peacock J. A., 1994, *ApJ*, 426, 23
 Feldman H. A., Frieman J. A., Fry J. N., Scoccimarro R., 2001, *Phys. Rev. Lett.*, 86, 1434
 Feldman H. A. et al., 2003, *ApJ*, 596, L131
 Fisher K. B., Nusser A., 1996, *MNRAS*, 279, L1
 Fisher K. B., Scharf C. A., Lahav O., 1994, *MNRAS*, 266, 219
 Fisher K. B., Lahav O., Hoffman Y., Lynden-Bell D., Zaroubi S., 1995, *MNRAS*, 272, 885
 Freedman W. L. et al., 2001, *ApJ*, 553, 47
 Hamilton A. J. S., Tegmark M., Padmanabhan N., 2000, *MNRAS*, 317, L23
 Hawkins E. et al., (the 2dFGRS team), 2003, *MNRAS*, 346, 78
 Heavens A. F., Taylor A. N., 1995, *MNRAS*, 275, 483 (HT)
 Hinshaw G. et al., (The *WMAP* Team), 2003, *ApJS*, 148, 135
 Jenkins A. et al., 1998, *ApJ*, 499, 20
 Juszkiewicz R., Ferreira P. G., Feldman H. A., Jaffe A. H., Davis M., 2000, *Sci*, 287, 109
 Lahav O. et al., (The 2dFGRS Team), 2002, *MNRAS*, 333, 961
 Lewis A., Bridle S., 2002, *Phys. Rev. D*, 66, 103511
 Lineweaver C. H., Tenorio L., Smoot G. F., Keegstra P., Banday A. J., Lubin P., 1996, *ApJ*, 470, 38
 Kaiser N., 1987, *MNRAS*, 227, 1
 Madgwick D. S. et al., (The 2dFGRS Team), 2003, *MNRAS*, 344, 847
 Norberg P. et al., (The 2dFGRS Team), 2001, *MNRAS*, 328, 64
 Norberg P. et al., (The 2dFGRS Team), 2002a, *MNRAS*, 332, 827
 Norberg P. et al., (The 2dFGRS Team), 2002b, *MNRAS*, 336, 907
 Page L. et al., (The *WMAP* Team), 2003, *ApJS*, 148, 233
 Peacock J. A. et al., (The 2dFGRS Team), 2001, *Nat*, 410, 169
 Peebles P. J. E., 1973, *ApJ*, 185, 413
 Percival W. J. et al., (The 2dFGRS Team), 2001, *MNRAS*, 327, 1297(P01)
 Percival W. J. et al., (The 2dFGRS Team), 2002, *MNRAS*, 337, 1068
 Percival W. J., Verde L., Peacock J. A., 2004, 347, 645
 Press W. H., Teukolsky S. A., Vetterling W. T., Flannery B. P., 1992, *Numerical recipes in C*, 2nd edn. Cambridge Univ. Press, Cambridge
 Refregier A., 2003, *Ann. Rev. Astron. Astrophys.*, 41, 645
 Saunders W. et al., 2000, *MNRAS*, 317, 55
 Smith R. E. et al., (Virgo consortium), 2003, *MNRAS*, 341, 1311

- Spergel D. N. et al., (The *WMAP* Team), 2003, *ApJS*, 148, 175
 Tadolos H. et al., 1999, *MNRAS*, 305, 527
 Taylor A. N., Ballinger W. E., Heavens A. F., Tadolos H., 2001, *MNRAS*, 327, 689
 Tegmark M., Taylor A. N., Heavens A. F., 1997, *ApJ*, 480, 22
 Tegmark M., Hamilton A. J. S., Xu Y., 2002, *MNRAS*, 335, 887
 Tegmark M. et al., 2004a, *ApJ*, 606, 702
 Tegmark M. et al., 2004b, *Phys. Rev. D*, 69, 103501
 Verde L. et al., (The 2dFGRS Team), 2002, *MNRAS*, 335, 432
 Verde L. et al., (The *WMAP* Team), 2003, *ApJS*, 148, 195
 Vogeley M. S., Szalay A. S., 1996, *ApJ*, 465, 34
 Wild V. et al., 2004, *MNRAS*, submitted (astro-ph/0404275)
 Zehavi I. et al., (The SDSS Team), 2002, *ApJ*, 571, 172

APPENDIX A: METHOD

The spherical harmonics method applied to the 2dFGRS in this paper has a number of significant differences from the formalisms developed for the *IRAS* surveys (Fisher et al. 1994, 1995; HT; Tadolos et al. 1999). The revisions are primarily due to the complicated geometry of the 2dFGRS survey (whereas the *IRAS* surveys nearly covered the whole sky), although we additionally apply a correction for varying galaxy bias, dependent on both galaxy luminosity and redshift. For these reasons we provide a simple, complete description of the formalism in this appendix. Note that throughout we use a single Greek subscript (e.g. ν) to represent a triplet (e.g. ℓ_ν, n_ν, m_ν), so the spherical harmonic $Y_\nu(\theta, \phi) \equiv Y_{\ell_\nu m_\nu}(\theta, \phi)$ and the spherical Bessel functions $j_\nu(s) \equiv j_{\ell_\nu}(k_{\ell_\nu n_\nu} s)$. $-\nu$ is defined to represent the triplet $(\ell_\nu, -m_\nu, n_\nu)$. We also adopt the following convention for coordinate positions: \mathbf{r} is the true (or real-space) position of a galaxy, \mathbf{s} is the observed redshift-space position given the linear infall velocity of the galaxy. \mathbf{s}' and \mathbf{r}' correspond to \mathbf{s} and \mathbf{r} including the systematic offset in the measured distance caused by the small-scale velocity dispersion of galaxies within larger virialized objects.

A1 Galaxy bias model

As in Lahav et al. (2002), we adopt a CGC model for the evolution of galaxy bias over the range of redshift covered by the 2dFGRS sample used in this analysis ($0 < z < 0.25$), i.e. we assume that the normalization of the galaxy density field is independent of redshift, for any galaxy luminosity L . We also assume that the relative expected bias $\hat{r}_b(L)$ of galaxies of luminosity L relative to that of L_* galaxies is a function of luminosity

$$\hat{r}_b(L) = \left\langle \frac{b(L, z)}{b(L_*, z)} \right\rangle = 0.85 + 0.15 \frac{L}{L_*}, \quad (\text{A1})$$

and that this ratio is independent of redshift. This dependence is implied by the relative clustering of 2dFGRS galaxies (Norberg et al. 2001).

In the analysis presented in this paper, the galaxy bias is modelled using a very simple linear form with the mean redshift-space density of galaxies of luminosity L given by

$$\rho(\mathbf{r}') = \bar{\rho}(\mathbf{r}') [1 + b(L, 0) \delta(\text{mass}, \mathbf{r}')] \quad (\text{A2})$$

$$= \bar{\rho}(\mathbf{r}') [1 + \hat{r}_b(L) \delta(L_*, \mathbf{r}')] , \quad (\text{A3})$$

where $\delta(\text{mass}, \mathbf{r}')$ is the present-day mass density field, and $\delta(L_*, \mathbf{r}')$ is the density field of galaxies of luminosity L_* , which is assumed to be independent of the epoch.

The galaxy bias model described above was used to correct the observed galaxy overdensity field, enabling measurement of the shape and amplitude of the power spectrum of L_* galaxies. Following the CGC model, we do not have to correct the recovered clustering

signal for evolution, provided that we wish to measure the galaxy rather than the mass power spectrum. However, because galaxy luminosity varies systematically with redshift, we do need to correct for luminosity-dependent bias, and we do this in a way analogous to the Fourier method presented by Percival et al. (2004), by weighting the contribution of each galaxy to the measured density field by the reciprocal of the expected bias ratio $\hat{r}_b(L)$ given by equation (A1). In the following description of the formalism, we only consider galaxies of luminosity L . Without loss of generality, this result can be expanded to cover a sample of galaxies with different luminosities by simply summing (or integrating) over the range of luminosities (as in Percival et al. 2004).

A2 The spherical harmonic formalism

Further description of the spherical harmonics formalism may be found in Fisher et al. (1994, 1995), HT and Tadolos et al. (1999). Expanding the density field of the redshift-space distribution of galaxies of luminosity L in spherical harmonics and spherical Bessel functions gives

$$\rho_\nu(L, \mathbf{s}') = c_\nu \int d^3 s' \frac{\rho(L, \mathbf{s}')}{\hat{r}_b(L)} w(\mathbf{s}') j_\nu(\mathbf{s}') Y_\nu^*(\theta, \phi), \quad (\text{A4})$$

where $w(\mathbf{s}')$ is a weighting function for which we adopt the standard Feldman et al. (1994) weight

$$w(\mathbf{s}') = \frac{1}{1 + \bar{\rho}(\mathbf{s}') \langle P(k) \rangle}. \quad (\text{A5})$$

Here, $\bar{\rho}(\mathbf{s}')$ is the mean galaxy redshift-space density for all galaxies, $\langle P(k) \rangle$ is an estimate of the power spectrum and \mathbf{s}' is the 3D redshift-space position variable. Note that, to simplify the procedure, we do not use luminosity-dependent weights as advocated by Percival et al. (2004). c_ν are normalization constants and $\rho(\mathbf{s}')$ is the galaxy redshift-space density. For a galaxy survey, $\rho(\mathbf{s}')$ is a sum of delta functions and the above integral decomposes to a sum over the galaxies.

The inverse transformation is given by

$$\frac{\rho(L, \mathbf{s}')}{\hat{r}_b(L)} w(\mathbf{s}') = \sum_\nu c_\nu \rho_\nu(L, \mathbf{s}') j_\nu(\mathbf{s}') Y_\nu(\theta, \phi). \quad (\text{A6})$$

Adopting the set of harmonics with

$$\left. \frac{d}{dr} j_\nu(r) \right|_{r_{\max}} = 0, \quad (\text{A7})$$

(i.e. with no boundary distortions at $r_{\max} = 706.2 h^{-1}$ Mpc), the normalization of the transform requires c_ν to satisfy

$$c_\nu^{-2} = \int d\mathbf{r} j_\nu^2(r) r^2. \quad (\text{A8})$$

A3 Small-scale velocity dispersion correction

We have applied the correction (described by HT) for the effect of the small-scale non-linear peculiar velocity field caused by the random motion of galaxies in groups. Because we are only interested in the large-scale linear power spectrum in this paper, the exact details of this correction are not significant (this is discussed further in Section 6.5). The effect of the velocity field is to smooth the observed overdensity field along the line of sight in a way that is equivalent to convolving with a matrix $S_{\nu\mu}$, i.e.

$$(\delta_{r'})_\nu = \sum_\mu S_{\nu\mu} (\delta_r)_\mu, \quad (\text{A9})$$

where

$$S_{v\mu} = c_v c_\mu \Delta_{\ell_v, \ell_\mu}^K \Delta_{m_v, m_\mu}^K \times \iint p(r-y) j_\mu(r) j_\nu(y) r dr y dy. \quad (\text{A10})$$

Here Δ^K is the Kronecker delta function and $p(r-y)$ is the one-dimensional scattering probability for the velocity dispersion. Models for $p(r-y)$ are given in equations (5)–(7), and the choice of model is discussed further in Section 6.5. Note that this formalism assumes that the induced dispersion is not a strong function of group mass.

A4 Modelling the transformed density field

The correction for luminosity-dependent bias given by equation (A1) is a function of galaxy properties, not the measured galaxy position. The galaxy density multiplied by this bias correction is therefore conserved with respect to a change in coordinates with number conservation implying

$$d^3 s' \frac{\rho(L, s')}{\hat{r}_b(L)} = d^3 r' \frac{\rho(L, r')}{\hat{r}_b(L)}. \quad (\text{A11})$$

The dependence of the redshift distortion term lies in the weighting and spherical Bessel functions and, following HT, we expand to first order in $\Delta r' \equiv s' - r'$,

$$w(s') j_\nu(s') \simeq w(r') j_\nu(r') + \Delta r' \frac{d}{dr} [w(r') j_\nu(r')]. \quad (\text{A12})$$

Using the Poisson equation to relate the gravitational potential with the density field

$$\Delta r'_{\text{lin}} = \Omega_m(z[r'])^{0.6} \times \sum_v \frac{1}{k_v^2} c_v \delta_v(\text{mass}, r') \frac{dj_\nu(r')}{dr} Y_\nu(\theta, \phi), \quad (\text{A13})$$

where $\delta_v(\text{mass}, r')$ is the transform of the mass overdensity field. As the linear redshift-space distortions are a function of the mass overdensity field, they are independent of galaxy luminosity. However, this means that they are expected to grow through the linear growth factor $D(z)$, normalized to $D(0) = 1$, within the CGC model. This and the redshift dependence of $\Omega_m(z)/\Omega_m(0)$ are calculated assuming a concordance model. We can now rewrite these distortions in terms of the transformed density field of galaxies of luminosity L_*

$$\Delta r'_{\text{lin}} = \frac{\Omega_m(z[r'])^{0.6}}{b(L_*, 0)} D(z[r']) \times \sum_v \frac{1}{k_v^2} c_v \delta_v(L_*, r') \frac{dj_\nu(r')}{dr} Y_\nu(\theta, \phi). \quad (\text{A14})$$

Defining

$$\beta(L_*, 0) \equiv \frac{\Omega_m(0)^{0.6}}{b(L_*, 0)}, \quad (\text{A15})$$

reduces this expression to

$$\Delta r'_{\text{lin}} = \beta(L_*, 0) \frac{\Omega_m(z[r'])^{0.6}}{\Omega_m(0)^{0.6}} D(z[r']) \times \sum_v \frac{1}{k_v^2} c_v \delta_v(L_*, r') \frac{dj_\nu(r')}{dr} Y_\nu(\theta, \phi). \quad (\text{A16})$$

Including a correction for the local group velocity \mathbf{v}_{LG} , assumed to be 622 km s^{-1} towards (B1950) RA = 162° , Dec. = -27° (Lineweaver et al. 1996; Courteau & van den Bergh 1999), gives

$$\Delta r' = \Delta r'_{\text{lin}} - \mathbf{v}_{LG} \cdot \hat{\mathbf{r}}'. \quad (\text{A17})$$

The local group velocity correction has a very minor effect on the results presented in this paper, but was included for completeness.

For galaxies of luminosity L , transforming the density field gives

$$\rho(L, \mathbf{r}') = \bar{\rho}(L, \mathbf{r}') \times \left[1 + \sum_v c_v \delta_v(L, \mathbf{r}') j_\nu(r') Y_\nu(\theta, \phi) \right], \quad (\text{A18})$$

where $\bar{\rho}(L, \mathbf{r}')$ is the observed mean density of galaxies of luminosity L in the survey. In fact, the mean number of galaxies as a function of the redshift-space distance $\bar{\rho}(L, s')$ is more easily determined than $\bar{\rho}(L, \mathbf{r}')$. It would be possible to reformulate the spherical harmonics formalism to use $\bar{\rho}(L, s')$ by separating the convolution of the window from the linear redshift-space distortion correction. Given the relatively small effect that the coordinate translation $\mathbf{r}' \rightarrow s'$ has on $\bar{\rho}(L, \mathbf{r}')$, we have instead chosen to use the original HT formalism with $\bar{\rho}(L, \mathbf{r}') \simeq \bar{\rho}(L, s')$ as measured from the survey. Converting from $\delta_v(L, \mathbf{r}')$ to consider the fluctuations traced by L_* galaxies gives

$$\rho(L, \mathbf{r}') = \bar{\rho}(L, \mathbf{r}') \times \left[1 + \sum_v c_v \hat{r}_b(L) \delta_v(L_*, r') j_\nu(r') Y_\nu(\theta, \phi) \right], \quad (\text{A19})$$

and we see that when we combine equations (A4) and (A19) to determine $\rho(L, \mathbf{r}')$ as a function of $\langle \delta_v(L_*, \mathbf{r}') \rangle$, the factors of $\hat{r}_b(L)$ in both these equations will cancel. Combining equations (A4), (A9), (A12), (A17) and (A19) gives

$$D_v \equiv \rho_v(L, \mathbf{r}') - \bar{\rho}_v(L, \mathbf{r}') - \rho_v(LG, \mathbf{r}') \quad (\text{A20})$$

$$= \sum_\mu [\Phi_{v\mu} + \beta(L_*, 0) V_{v\mu}] \delta_\mu(L_*, r') \quad (\text{A21})$$

$$= \sum_\mu \sum_\eta [\Phi_{v\mu} + \beta(L_*, 0) V_{v\mu}] S_{\mu\eta} \delta_\eta(L_*, r) \quad (\text{A22})$$

where the mean-field harmonics are defined as

$$\bar{\rho}_v(L, \mathbf{r}') = c_v \int d^3 r' \frac{\bar{\rho}(L, \mathbf{r}')}{\hat{r}_b(L)} w(r') j_\nu(r') Y_\nu^*(\theta, \phi), \quad (\text{A23})$$

the local group contribution is given by

$$\rho_v(LG, \mathbf{r}') = c_v \int d^3 r' (\mathbf{v}_{LG} \cdot \hat{\mathbf{r}}') \frac{\bar{\rho}(L, \mathbf{r}')}{\hat{r}_b(L)} \times \frac{d}{dr} [w(r') j_\nu(r')] Y_\nu^*(\theta, \phi), \quad (\text{A24})$$

and the Φ and V matrices are defined as

$$\Phi_{v\mu} = c_v c_\mu \int d^3 r' \bar{\rho}(L, \mathbf{r}') w(r') j_\nu(r') j_\mu(r') \times Y_\nu^*(\theta, \phi) Y_\mu(\theta, \phi) \quad (\text{A25})$$

and

$$V_{v\mu} = \frac{c_v c_\mu}{k_\mu^2} \int d^3 r' \frac{\bar{\rho}(L, \mathbf{r}')}{\hat{r}_b(L)} \frac{\Omega_m(z)^{0.6}}{\Omega_m(0)^{0.6}} D(z) \times \frac{d}{dr'} [w(r') j_\nu(r')] \frac{d}{dr'} j_\mu(r') Y_\nu^*(\theta, \phi) Y_\mu(\theta, \phi). \quad (\text{A26})$$

Assuming that the mean observed density field $\bar{\rho}(L, \mathbf{r}') = \bar{\rho}(L, r') M(\theta, \phi)$ and the weighting $w(\mathbf{r}') = w(r') w(\theta, \phi)$ can be

split into angular and radial components, then the 3D integrals required to calculate the Φ and V matrices have the same angular contribution

$$W_{\nu\mu} = \int d\theta d\phi w(\theta, \phi) Y_{\nu}^*(\theta, \phi) M(\theta, \phi) Y_{\mu}(\theta, \phi), \quad (\text{A27})$$

where $M(\theta, \phi)$ is the sky mask of the survey. This therefore only needs to be calculated once.

The effect of the survey geometry (matrix $\Phi_{\nu\mu}$) is independent of the luminosity-dependent bias correction: the $1/\hat{r}_b(L)$ factor in equation (A4) was designed to cancel the offset in $\delta(L, \mathbf{r}')$ (equation A3). Note that we have included the redshift evolution part of $\beta(L_*, z)$ in equation (A26), and in the calculation performed, so that we fit the data with $\beta(L_*, 0)$. Ignoring this correction gives a measured $\beta(L_*, z)$ approximately 10 per cent larger than $\beta(L_*, 0)$, because it corresponds to an effective redshift ~ 0.17 .

A5 Construction of the covariance matrix

In this section we only work with the real-space position, and all overdensities correspond to L_* galaxies. For simplicity, we therefore define $\delta_{\mu} \equiv \delta_{\mu}(L_*, \mathbf{r}')$. We also define

$$\Psi_{\nu\mu} \equiv \sum_{\eta} (\Phi_{\nu\eta} + \beta(L_*, 0) V_{\nu\eta}) S_{\eta\mu}, \quad (\text{A28})$$

so that equation (A22) becomes

$$D_{\nu} = \sum_{\mu} \Psi_{\nu\mu} \delta_{\mu}. \quad (\text{A29})$$

The real and imaginary parts of D_{ν} are given by

$$\text{Re } D_{\nu} = \sum_{\eta} (\text{Re } \Psi_{\nu\eta} \text{Re } \delta_{\eta} - \text{Im } \Psi_{\nu\eta} \text{Im } \delta_{\eta}) \quad (\text{A30})$$

$$\text{Im } D_{\nu} = \sum_{\eta} (\text{Im } \Psi_{\nu\eta} \text{Re } \delta_{\eta} + \text{Re } \Psi_{\nu\eta} \text{Im } \delta_{\eta}). \quad (\text{A31})$$

From equations (A28) and (A29) it can be seen that, for a single mode, the expected value $\langle \text{Re } D_{\nu} \text{Re } D_{\mu} \rangle$ or $\langle \text{Im } D_{\nu} \text{Im } D_{\mu} \rangle$ can be split into three components dependent on $\beta(L_*, 0)^n$ with $n = 0, 1, 2$.

Given the large number of modes within the linear regime, rather than estimating the covariances of all modes, we reduce the problem to considering a number of combinations of the real and imaginary parts of D_{ν} . We will discuss how we optimally chose the direction of the component vectors in the space of all modes in Section A7. Suppose the revised mode combinations that we wish to consider are given by

$$\hat{D}_a = \sum_{\nu} E_{a\nu}^r \text{Re } D_{\nu} + \sum_{\nu} E_{a\nu}^i \text{Im } D_{\nu}. \quad (\text{A32})$$

Note that here a does not represent a triplet of ℓ , m and n , but is instead simply an index of the modes chosen. Using equations (A30) and (A31), we can decompose into multiples of the real and imaginary components of δ

$$\hat{D}_a = \sum_{\eta} (\Upsilon_{a\eta}^r \text{Re } \delta_{\eta} + \Upsilon_{a\eta}^i \text{Im } \delta_{\eta}), \quad (\text{A33})$$

where

$$\Upsilon_{a\eta}^r = \sum_{\nu} (E_{a\nu}^r \text{Re } \Psi_{\nu\eta} + E_{a\nu}^i \text{Im } \Psi_{\nu\eta}) \quad (\text{A34})$$

$$\Upsilon_{a\eta}^i = \sum_{\nu} (E_{a\nu}^i \text{Re } \Psi_{\nu\eta} - E_{a\nu}^r \text{Im } \Psi_{\nu\eta}). \quad (\text{A35})$$

The expected values of $\langle \hat{D}_a \hat{D}_b \rangle$ are then

$$\langle \hat{D}_a \hat{D}_b \rangle = \sum_{\eta} \sum_{\gamma} \langle (\Upsilon_{a\eta}^r \text{Re } \delta_{\eta} + \Upsilon_{a\eta}^i \text{Im } \delta_{\eta}) \times (\Upsilon_{b\gamma}^r \text{Re } \delta_{\gamma} + \Upsilon_{b\gamma}^i \text{Im } \delta_{\gamma}) \rangle. \quad (\text{A36})$$

Assuming a standard Gaussian density field, the double sum in equation (A36) can be reduced to a single sum using the following relations

$$\langle \text{Re } \delta_{\nu} \text{Im } \delta_{\mu} \rangle = 0 \quad (\text{A37})$$

$$\langle \text{Re } \delta_{\nu} \text{Re } \delta_{\mu} \rangle = [\Delta_{\nu,\mu}^K + (-1)^{m_{\nu}} \Delta_{\nu,-\mu}^K] \frac{P(k_{\nu})}{2} \quad (\text{A38})$$

$$\langle \text{Im } \delta_{\nu} \text{Im } \delta_{\mu} \rangle = [\Delta_{\nu,\mu}^K - (-1)^{m_{\nu}} \Delta_{\nu,-\mu}^K] \frac{P(k_{\nu})}{2}, \quad (\text{A39})$$

where the $\Delta_{\nu,\mu}^K$ terms arise because δ_{ν} obeys the Hermitian relation $\delta_{\nu}^* = (-1)^{m_{\nu}} \delta_{-\nu}$. These terms are only important for geometries that lack azimuthal symmetry, such as the 2dFGRS and are less important for the PSCz survey. The dependence on $P(k)$ follows because the transformation from the Fourier basis to the spherical harmonics basis is unitary and the amplitude of the complex variable is unchanged. Using these relations, equation (A36) reduces to

$$\langle \hat{D}_a \hat{D}_b \rangle = \sum_{\eta} \frac{P(k_{\eta})}{2} [\Upsilon_{a\eta}^r \Upsilon_{b\eta}^r + \Upsilon_{a\eta}^i \Upsilon_{b\eta}^i + (-1)^{m_{\eta}} \Upsilon_{a\eta}^r \Upsilon_{b-\eta}^r - (-1)^{m_{\eta}} \Upsilon_{a\eta}^i \Upsilon_{b-\eta}^i]. \quad (\text{A40})$$

This equation gives the geometrical component of the covariance matrix resulting from the mixing of modes caused by the survey geometry and large-scale redshift-space distortions. Note that, by substituting equations (A28), (A34) and (A35) into this equation we could split the geometric part of the covariance matrix into three components with varying dependence on $\beta(L_*, 0)$. This is actually the case in our implementation of the method so we only have to calculate these three components once for any value of $\beta(L_*, 0)$.

In addition, there is a shot noise component which can be calculated by the methods of Peebles (1973). This term enters into the above formalism because the density field $\rho(L, \mathbf{s}')$ in equation (A4) is actually the sum of a series of delta functions, each at the position of a galaxy. The expected value of $\langle D_{\mu} D_{\nu} \rangle$ therefore includes two terms (as in appendix A of Feldman et al. 1994) corresponding to the convolved power and the shot noise. Allowing a and b to represent either real or imaginary parts, the expected value of the noise component for each mode, for a particular galaxy luminosity is

$$\langle a N_{\nu} b N_{\mu} \rangle = c_{\nu} c_{\mu} \int d^3r \frac{\bar{\rho}(L, \mathbf{r})}{\hat{r}_b^2(L)} w^2(\mathbf{r}) j_{\nu}(r) j_{\mu}(r) r^2 \times a Y_{\nu}^*(\theta, \phi) b Y_{\mu}^*(\theta, \phi). \quad (\text{A41})$$

To allow for all galaxy luminosities, we simply integrate over luminosity as in Percival et al. (2004).

Allowing for the combinations of modes defined in equation (A32)

$$\langle \hat{N}_a \hat{N}_b \rangle = \sum_{\nu} \sum_{\mu} (E_{a\nu}^r E_{b\mu}^r \langle \text{Re } N_{\nu} \text{Re } N_{\mu} \rangle + E_{a\nu}^i E_{b\mu}^i \langle \text{Im } N_{\nu} \text{Im } N_{\mu} \rangle + E_{a\nu}^r E_{b\mu}^i \langle \text{Re } N_{\nu} \text{Im } N_{\mu} \rangle + E_{a\nu}^i E_{b\mu}^r \langle \text{Im } N_{\nu} \text{Re } N_{\mu} \rangle). \quad (\text{A42})$$

The components of the covariance matrix of the reduced data are $\langle \hat{D}_a \hat{D}_b \rangle + \langle \hat{N}_a \hat{N}_b \rangle$ as given by equations (A40) and (A42).

A6 Some practical issues

The calculation of the angular part of the mixing matrices, $W_{\nu\mu}$ (given by equation A27) is more CPU intensive than the calculation of the radial components. As a result of this, Tadros et al. (1999) utilized Clebsch–Gordan matrices to relate a single transform of the angular mask to the full transition matrix given by equation (A27). However at the high ℓ values required for the complex geometry of the 2dFGRS survey it is computationally expensive to calculate these accurately. As the integral in equation (A27) can be reduced to a sum over the angular mask, a direct integration proved stable and computationally faster than the more complicated Clebsch–Gordan method. At low- ℓ values both methods agreed to a sufficient level of precision.

In the large-scale regime $k < 0.15 h \text{ Mpc}^{-1}$, and in the regime where the assumed redshift distribution does not have a significant effect on the recovered power $k > 0.02 h \text{ Mpc}^{-1}$ (see P01), there are 86 667 modes with $m \geq 0$. This statistically complete set includes real and imaginary modes separately, but only includes modes with $m \geq 0$ because D_ν (equation A22) obeys the Hermitian relation and positive and negative m modes are degenerate. The maximum n of the modes in this set is 33, and the maximum ℓ is 101.

Obviously we cannot invert a $86\,667 \times 86\,667$ covariance matrix with each mode as a single element for every model we wish to test, and we therefore need to reduce the number of modes compared. Another serious consideration is that many of the modes are nearly degenerate. As we can only calculate the components required with finite precision, nearly degenerate modes often become completely degenerate due to numerical issues and therefore need to be removed from the analysis: covariance matrices with negative eigenvalues are unphysical. Removing degenerate modes is discussed in the context of data compression in the next subsection.

There are two convolutions that we need to perform to determine the covariance matrix, given by equations (A28) and (A29). The number of modes summed when numerically performing these convolutions is limited by computational time. The first convolution is given by equation (A28) and results from the small-scale velocity dispersion correction. This convolution is a simple convolution in n and is relatively narrow in the linear regime that we consider in this paper. In fact we chose to convolve over $1 \leq n \leq 100$. The second convolution is given by equation (A40), and is performed for $\ell \leq 200$. This is complete for $k < 0.29 h \text{ Mpc}^{-1}$, and contains $>4 \times 10^6$ modes. A limit in ℓ was chosen rather than a limit in k as the CPU time taken to perform the convolution is dependent on ℓ_{max} . The k distribution of contributions to a few of the chosen modes is presented in Fig. A1. Note that although the convolved set of modes is complete for $k < 0.29 h \text{ Mpc}^{-1}$, the fall-off to higher k is very gentle, and most of the signal beyond this limit will still be included in the convolution.

A7 Data compression

As mentioned in Section A6, there are 86 667 spherical harmonic modes with $0.02 < k < 0.15 h \text{ Mpc}^{-1}$, and it is impractical to use all of these modes in a likelihood analysis. Consequently, we reject modes for the following reasons.

(i) The 2dFGRS regions considered have a relatively small azimuthal angle, so modes that are relatively smooth in this direction will be close to degenerate. We therefore set a limit of $\ell - |m| > 5$ for the modes analysed. This limit effectively constrains the number of azimuthal wavelengths in the modes used.

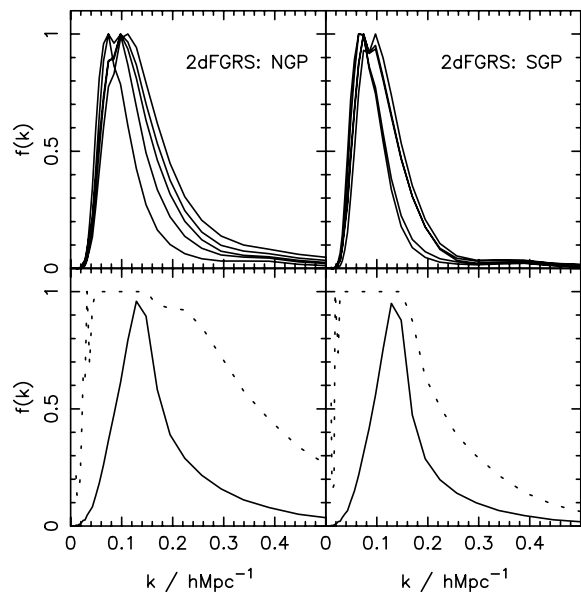


Figure A1. Normalized contribution to $P(k)$ as a function of k for five example modes for the NGP and SGP (top row). In the lower row we present the average (solid line) and maximum (dotted line) of the normalized distribution of k contributions, calculated from all modes used.

(ii) Modes with similar ℓ values were found to be closely degenerate. Rather than applying a more optimal form of data compression, it was decided to simply sample the range of ℓ values with $\Delta\ell = 10$. This spacing was chosen by examining the number of small eigenvalues in the three components of the covariance matrix as described after equation (A40).

In addition, we carry out the following steps to remove degenerate modes in the covariance matrix and to compress the data further. These steps are performed first in the angular direction (assuming modes with different ℓ and n values are independent), then on all of the remaining modes.

(i) Even after rejection of near ℓ values, nearly degenerate combinations of modes remain, which, given the limited numerical resolution achievable, could give negative eigenvalues in the covariance matrix. As a result of this, only modes with eigenvalues in the covariance matrix greater than 10^{-5} times the maximum eigenvalue, well above the round-off error, are retained in the three components of the covariance matrix as described after equation (A40). This step is effectively a principal-component reduction of the covariance matrix eigenvectors.

(ii) Finally, we perform a KL decomposition of the covariance matrix optimized to constrain $\beta(L_*, 0)$. After our angular reduction we retain 2155 and 2172 modes for the NGP and SGP respectively after this step. Following radial compression we are left with 1223 and 1785 modes for the NGP and SGP, respectively. The number of modes retained for the NGP is smaller than for the SGP because the smaller angular coverage means that more modes are nearly degenerate.

A8 Calculating the likelihood

Following the hypothesis that $\text{Re } D_\nu$ and $\text{Im } D_\nu$ are Gaussian random variables, the likelihood function for the variables of interest

can be written as

$$\mathcal{L}[\mathbf{D}|\beta(L_*, 0), P(k)] = \frac{1}{(2\pi)^{N/2}|\mathbf{C}|^{1/2}} \exp\left(-\frac{1}{2}\mathbf{D}^T\mathbf{C}^{-1}\mathbf{D}\right). \quad (\text{A43})$$

Matrix inversion is an N^3 process, so finding the inverse covariance matrix can be prohibitively slow in order to test a large number of models. However, the KL procedure described in Section A7 means that the covariance matrix is diagonal for a model chosen to be close to the best-fitting position. To the first order, we might be tempted to assume that the covariance matrix is diagonal over the range of models to be tested. However, this can bias the solution depending on the exact form of the matrix. A compromise is to apply the iterative Newton–Raphson method of root finding to matrix inversion (section 2.2.5 of Press et al. 1992) starting with the diagonal inverse covariance matrix as the first estimate. Given an estimate of the inverse covariance matrix H_0 , our revised estimate is $H_1 = 2H_0 - H_0CH_0$. As H_0 is diagonal, the first step of this iterative method only takes of order N^2 operations. This trick allows the likelihood to

be quickly calculated for a large number of models, and we use this method in Section 5.2, when we consider a fixed power spectrum shape.

However, over the larger range of models considered in Section 5.3, the covariance matrix changes significantly, and the estimate H_1 is not sufficiently accurate. Instead, a full matrix inversion is performed for each model, so mapping the likelihood hypersurface becomes computationally expensive. A fast method for mapping surfaces which has recently become fashionable in cosmology is the Markov-chain Monte Carlo technique, where an iterative walk is performed in parameter space seeking local likelihood maxima (e.g. Lewis & Bridle 2002; Verde et al. 2003; Tegmark et al. 2003b). However, we only wish to consider a variation of four parameters ($\beta(L_*, z)$, $b(L_*, 0)\sigma_8$, $\Omega_m h$ and Ω_b/Ω_m) in a very simple model described in Section 5.1, so it is easy to map the likelihood surface using a grid.

This paper has been typeset from a $\text{\TeX}/\text{\LaTeX}$ file prepared by the author.